Carbohydrate Polymers 344 (2024) 122522

Contents lists available at ScienceDirect

Carbohydrate Polymers

journal homepage: www.elsevier.com/locate/carbpol

Zn@TA assisted dual cross-linked 3D printable glycol grafted chitosan hydrogels for robust antibiofilm and wound healing

Tejal V. Patil [a,b,1], Hexiu Jin [c,1], Sayan Deb Dutta [a,e], Rumi Aacharya [a,b], Kehan Chen [c], Keya Ganguly [a,d], Aayushi Randhawa [a,b], Ki-Taek Lim [a,b,d,*]

[a] Department of Biosystems Engineering, Kangwon National University, Chuncheon-24341, Republic of Korea
[b] Interdisciplinary Program in Smart Agriculture, Kangwon National University, Chuncheon-24341, Republic of Korea
[c] Department of Plastic and Traumatic Surgery, Capital Medical University, Beijing-10096, China
[d] Institute of Forest Science, Kangwon National University, Chuncheon-24341, Republic of Korea
[e] Center for Surgical Bioengineering, Department of Surgery, School of Medicine, University of California Davis, Sacramento, California-95817, United States

ARTICLE INFO

Keywords:
Chitosan
Zinc-tannic acid
Multifunctional hydrogel
3D printing
Antibacterial
Wound healing

ABSTRACT

Rapid regeneration of the injured tissue or organs is necessary to achieve the usual functionalities of the damaged parts. However, bacterial infections delay the regeneration process, a severe challenge in the personalized healthcare sector. To overcome these challenges, 3D-printable multifunctional hydrogels of Zn/tannic acid-reinforced glycol functionalized chitosan for rapid wound healing were developed. Polyphenol strengthened intermolecular connections, while glutaraldehyde stabilized 3D-printed structures. The hydrogel exhibited enhanced viscoelasticity (G′; 1.96×10^4 Pa) and adhesiveness (210 kPa). The dual-crosslinked scaffolds showed remarkable antibacterial activity against *Bacillus subtilis* (~81 %) and *Escherichia coli* (92.75 %). The hydrogels showed no adverse effects on human dermal fibroblasts (HDFs) and macrophages (RAW 264.7), indicating their superior biocompatibility. The Zn/TA-reinforced hydrogels accelerate M2 polarization of macrophages through the activation of anti-inflammatory transcription factors (*Arg-1*, *VEGF*, *CD163*, and *IL-10*), suggesting better immunomodulatory effects, which is favorable for rapid wound regeneration. Higher collagen deposition and rapid re-epithelialization occurred in scaffold-treated rat groups vis-à-vis controls, demonstrating superior wound healing. Taken together, the developed multifunctional hydrogels have great potential for rapidly regenerating bacteria-infected wounds in the personalized healthcare sector.

1. Introduction

Bacterial infections pose a significant threat to human health (Mora et al., 2022), particularly targeting open wounds and organs with compromised immunity (Zhang et al., 2023). The discovery of antibiotics in the twentieth century marked a crucial milestone in the fight against bacterial infections, initiating what is known as the antibiotic era. Initially celebrated for their efficacy in killing bacteria with minimal toxicity to animals, antibiotics soon faced a formidable challenge as bacteria developed tolerance and resistance to them. Recent research by the World Health Organization (WHO) indicates that resistant bacteria are responsible for an estimated 7.7 billion deaths annually worldwide, with projections suggesting a staggering increase to 10 million deaths by 2050, surpassing cancer-related mortality rates (ReAct, 2022). Given their remarkable capacity for antibiotic resistance and tolerance, this escalating threat underscores the urgent need to develop effective strategies to combat bacterial infections. Addressing bacterial infections effectively necessitates the development of materials capable of promoting tissue engineering and wound healing while circumventing antibiotic resistance mechanisms. Extensive research efforts have been dedicated to exploring biomaterials with properties aimed at overcoming antibiotic resistance, inhibiting bacterial adhesion, eradicating microorganisms, and preventing biofilm formation (Sahli et al., 2022). Various approaches have been employed, including fabricating antibacterial surfaces through polymeric coatings, metallic nanoparticles, and nature-inspired materials using technologies such as solvent casting, electrospinning, freeze-drying, gas foaming, and 3D printing (Alsahag et al., 2023; Dong et al., 2022; Liu et al., 2022; Pillai et al., 2022). Among

* Corresponding author at: Department of Biosystems Engineering, Kangwon National University, Chuncheon-24341, Republic of Korea.
E-mail address: ktlim@kangwon.ac.kr (K.-T. Lim).
[1] Authors contributed equally to this manuscript.

https://doi.org/10.1016/j.carbpol.2024.122522
Received 25 March 2024; Received in revised form 11 July 2024; Accepted 17 July 2024
Available online 22 July 2024

these techniques, 3D-printed scaffolds offer distinct advantages, including cost-effectiveness, rapid prototyping, customizable designs, and enhanced potential for cell proliferation, essential for accelerated wound healing (Tabriz & Douroumis, 2022; Xu et al., 2018).

Chitosan, with its promising properties in tissue engineering and antimicrobial activity, emerges as a compelling candidate for biomedical applications. While its biocompatibility, biodegradability, and mucoadhesivity render it suitable for regenerative medicine scaffolds, challenges include limited mechanical strength and variable antibacterial activity based on molecular weight and degree of deacetylation (Yadav et al., 2023). These limitations can potentially be addressed through chemical modification or composite strategies. Gelatin, a vital component of the extracellular matrix, enhances cell adhesion, proliferation, and migration but faces hurdles such as poor mechanical properties and inadequate antibacterial activity (Choi & Cha, 2019). Combining gelatin and chitosan presents an innovative approach to surmounting these challenges, as demonstrated in previous studies. Han and colleagues investigated an oligochitosan-gelatin-based suture with curcumin encapsulated by poly(lactic-*co*-glycolic acid) and tannic acid formulation (Han et al., 2023). While this electroactive suture facilitated scar-free wound healing and offered sustained drug release, its synthesis process proved cumbersome, involving multiple chemicals. This drug-dependent suture might restrict its applicability, especially in scenarios where bacteria develop tolerance or resistance to the drug. Moreover, further investigation into its antibacterial, antibiofilm, and antioxidant properties is necessary to determine its potential for future applications. In another study, He et al. synthesized adhesive hydrogels using methacrylated chitosan and gelatin grafted with protocatechuic

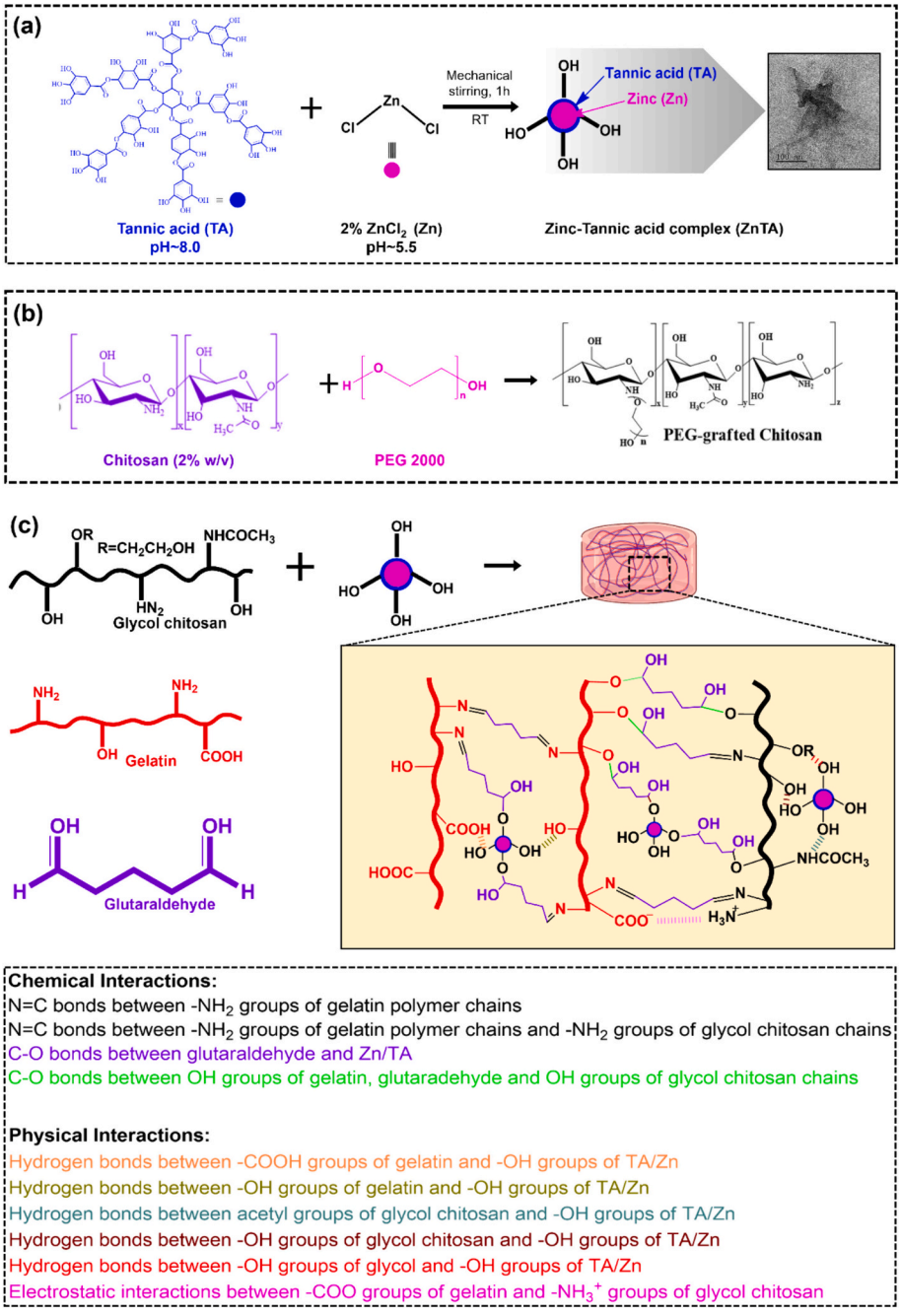

Scheme 1. Schematic presentation of fabrication of GC/ZT hydrogels: (a) Functionalization of Zn with TA (ZnTA complex), (b) Grafting of PEG moiety with chitosan, and (c) Development of multifunctional GC/ZT hydrogel using PEG grafted-chitosan and ZnTA complex with their possible interactions.

acid and dopamine hydrochloride by EDC-NHS-mediated coupling (He et al., 2020). The developed hydrogels exhibited excellent antibacterial properties and facilitated infected wound healing. However, compared to the convenient storage and respiration benefits of 3D-printed structures at wound sites, the storage and handling of developed hydrogels pose challenges.

In addition to addressing antibiotic resistance, incorporating antioxidant materials into biomedical scaffolds presents a multifaceted approach to combating bacterial infections and promoting chronic wound healing (Lobo et al., 2010). Tannic acid (TA), a polyphenol with diverse pharmacological properties, holds promise for biomedical applications due to its biosafety, biocompatibility, and biodegradability (Bigham et al., 2022). The free gallic acid groups of tannic acid can form multiple interactions, including hydrogen bonds and π-π bonds, by coordinating with metal ions to create metal-TA supramolecular amorphous networks (Chen et al., 2022). Metallic ions like zinc, copper, silver, gold, and iron are attractive scaffold builders and benefit cells in trace amounts (Alvarez & Nakajima, 2009). Zn^{2+} ions activate platelets, cell adhesion, differentiation, and antibacterial activity, and also modulate macrophage polarization towards an anti-inflammatory phenotype, which is crucial for promoting tissue regeneration (Huang et al., 2023; Liu et al., 2018).

Building upon these insights, we propose the development of gelatin/glycol chitosan/zinc-tannic acid (GC/ZT) hydrogels with enhanced antibacterial and antioxidant properties and 3D printability for wound healing applications. Scheme 1 illustrates the fabrication process of GC/ZT hydrogels alongside their interactions between glycol chitosan, gelatin, glutaraldehyde, and the ZnTA complex. The applications of 3D-printed hydrogels are schematically presented in Scheme 2. The hydrogels exhibit desirable characteristics such as printability, adhesiveness, and viscoelasticity. Glycol chitosan improves the antibacterial and antibiofilm properties of gelatin matrices. The added ZnTA enhances the antioxidant properties and promotes cell proliferation and migration. Our hypothesis suggests that these multifunctional scaffolds could represent a promising advancement in healthcare, offering a solution to expensive fabrication and critical challenges and improving patient outcomes.

2. Experimental section

2.1. Materials and reagents

The following chemicals were used in the experiments: gelatin (gel strength 300, type A, 70–90 % protein, Sigma-Aldrich, St. Louis, USA), chitosan (MW: 310–375 kDa, >75 % deacetylated, Sigma-Aldrich, St. Louis, Massachusetts, USA), tannic acid (ACS reagent, Sigma-Aldrich, St. Louis, Massachusetts, USA), 2, 2-Diphenyl-1-picrylhydrazyl (DPPH) (Sigma Aldrich, St. Louis, Massachusetts, USA), anhydrous zinc chloride (99.95 % purity, Thermo Scientific, USA), propidium iodide and SYTO9 (Invitrogen, Seoul, Republic of Korea), and polyethylene glycol (PEG) 2000 (Alfa Aesar, Belgium, Europe). *Escherichia coli* and *Bacillus subtilis* were provided from Korean Collection of Type Cultures (KCTC) (Jeonbuk, Republic of Korea). WST-8 kit (Cellrix®, MediFab Co., Ltd., Seoul, Republic of Korea), human dermal fibroblasts (HDF), and RAW 264.7 were purchased from American Type Cell Culture (ATCC) (Manassas, Virginia, USA). All chemicals were used as purchased without any additional purification.

2.2. Synthesis of ZnTA complex and PEG-grafted chitosan

For the ZnTA complex, 2 % zinc chloride solution (pH ~5.5) was dropwise added into the 4 % (*w/v*) tannic acid solution (pH ~8.0) and continuously stirred for 1 h at room temperature. After that, the precipitate was filtered, washed with distilled water (4 times), and dried at 45 °C for 4–5 days. The PEG-grafted chitosan was prepared as previously reported elsewhere with slight modifications (Zhang et al., 2002). In brief, a 2 % (w/v) chitosan solution was homogeneously prepared in 2 % acetic acid, followed by the addition of equal amounts of PEG and continuous stirring for 2 h at room temperature. After that, the resultant solution was dialyzed against distilled water for 4–5 days, followed by freeze-drying.

2.3. Hydrogel formulation

Gelatin (10 % w/v) and glycol chitosan (5 % w/v) were added to 1 % acetic acid and stirred magnetically at 60 °C until a homogeneous mixture was obtained. 1 %, 2 %, and 4 % (*w*/w) of ZnTA (w.r.t. total weight of gelatin/glycol chitosan) were added to obtain GC/ZT-1, GC/ZT-2, and GC/ZT-4 hydrogels. Samples without ZnTA particles were denoted at GC/ZT-0. The components and their composition are summarized in the **Supplementary Information (SI) Table S1.**

2.4. Hydrogel printing

All hydrogels were printed using the CELLINK BIO-X printer with controlled nozzle and platform temperatures. Printing conditions are mentioned in **Table S2**. After printing, scaffolds underwent overnight incubation at 4 °C for primary crosslinking, followed by immersion in 1

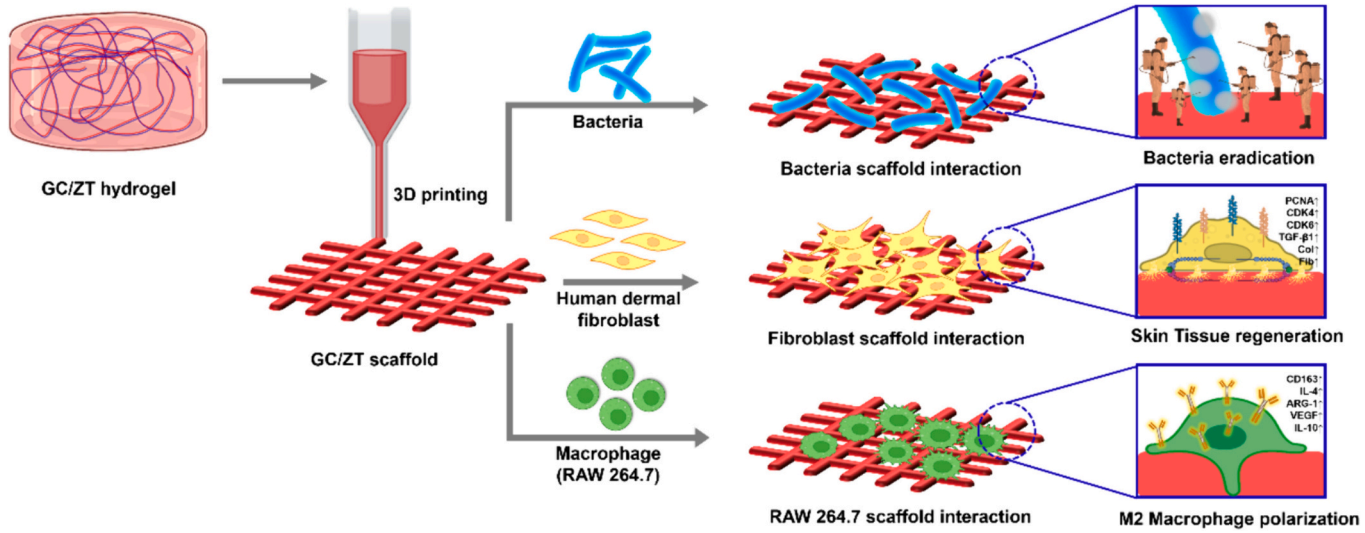

Scheme 2. Schematic presentation of 3D printed GC/ZT hydrogels and application in bacteria inhibition, tissue regeneration, and macrophage polarization.

% glutaraldehyde for chemical crosslinking. Scaffolds were then washed, freeze-dried for 2 days, and used for characterization. Printability was assessed based on the expansion ratio, uniformity factor, and integrity factor using the equations given below.

$$\text{Expansion ratio } (\alpha) = \frac{\text{Diamter of the filament (d)}}{\text{Diamter of the nozzle (D)}}$$

$$\text{Uniformity factor (U)} = \frac{\text{Length of the printed structure } (L_p)}{\text{Length of the of theoretical strand } (L_t)}$$

$$\text{Integrity factor (U)} = \frac{\text{Thickness of the printed structure } (T_p)}{\text{Thickness of the theoretical strand } (T_t)}$$

2.5. Characterization

The various analytical tools, including proton NMR, SEM, EDS, TEM, AFM, FTIR, XRD, and XPS, were explored to examine the physicochemical properties of the functionalized chitosan, tannic acid, and developed hydrogel scaffolds. The detailed information about characterization is given in the **SI** section.

2.6. Adhesive properties of hydrogels

The universal testing measurement (UTM; MCT-1150, AND Inc., Japan) equipment was used to investigate the adhesive strength of the hydrogel at room temperature using the lap-shear technique (Patel et al., 2023). Briefly, the hydrogel of equal weight (70 mg) was sandwiched between two 4.5 × 1.2 cm cardboard surfaces and left to dry for 20 min. Later, the pulling force was applied from opposite sides, and UTM recorded the data. A similar experiment was performed with porcine skin to check the adhesiveness of the skin surface.

2.7. Wettability and degradation study

The hydrophilicity of the samples was analyzed using a static contact angle instrument (Phoenix-MT, Komachine, Suwon, Republic of Korea). A film of GC/ZT-0, GC/ZT-1, GC/ZT-2, and GC/ZT-4 hydrogels was prepared for water contact angle measurement. ~5 μL of distilled water was dropped on the film surface, and the contact angle was measured immediately.

To analyze the degradation of 3D-printed structures, scaffolds with equal weights were immersed in 1 mL of 1× PBS and kept at a 100 rpm rotation condition. Each scaffold was removed from the solution at predetermined intervals, and the weight was recorded. The mass loss of samples was calculated using the below formula:

$$\textit{Mass loss} = \frac{\textit{Initial weight of the sample} - \textit{Final weight of the sample}}{\textit{Initial weight of the sample}} \times 100$$

2.8. Antioxidant, antibacterial and anti-biofilm efficiency

The reactive oxygen species scavenging activity of GC/ZT hydrogels was studied by measuring its activity against DPPH radicals. Scaffolds with equal weights were dipped in 0.5 mL of a 0.1 mM DPPH solution and preserved in the dark. The absorbance of samples was measured at a wavelength of 517 nm by a spectrophotometer (Tecan Infinite 200 Pro, Mannedorf, Switzerland) after 30 min, 1 h, and 2 h. The antibacterial and anti-biofilms potentials of the developed hydrogels were examined against *Escherichia coli* (*E. coli*) and *Bacillus subtilis* (*B. subtilis*). Details are provided in the **SI** section. Zinc release study is also given in the **SI** section.

2.9. Biocompatibility analysis

2.9.1. Cell viability and migration

The biocompatibility of the developed materials was examined with Human dermal fibroblast (HDF) cells and macrophages (RAW 264.7). The primary process of cell culture is given in **SI.** For cell viability, 1×10^4 cells (HDFs and macrophages) were seeded on the surface of the cross-linked scaffolds and incubated for 1, 3, and 5 days. The old media was changed every 3-day interval. After incubation, 100 μL of WST-8 reagent was added and incubated for 2 h at 37 °C in a CO_2 incubator. The absorbance was recorded at 450 nm using a spectrophotometer. All experiments were performed in triplicate ($n = 3$). For cell migration, 2×10^4 HDF cells were added to 6 well plates containing the hydrogel-extracted media and allowed to grow until confluent. After that, the monolayer cells were scratched using a 1 mL sterile tip, and the detached cells were removed by washing with 1 × PBS (4 times). The images of migrated cells were captured at 0 and 24 h using an optical microscope (Zeiss Optical Microscope, Germany). The detailed processes of qRT-PCR, immunocytochemistry, and macrophage polarization and their gene expression are given in the **SI** section.

2.9.2. In vivo analysis

In vivo investigation was conducted to evaluate the wound-healing capabilities of the scaffolds. The Institutional Animal Care and Use Committee (IACUC) at Capital Medical University in Beijing, China, approved all surgical procedures that followed the National Research Council's Guidelines for the Care and Use of Laboratory Animals. The surgical procedures were authorized by the Animal Experimental and Ethical Committee (Permission No. KQYY-202012-004). A group of male rats with an average weight between 42 and 52 g was obtained from the Institute of Cancer Research (ICR) (total number of rats = 9). The experiment was divided into three groups: a negative group (without treatment), group 1 labeled GC/ZT-0, and group 2 labeled GC/ZT-4. We selected the GC/ZT-0 and GC/ZT-4 scaffolds for *in vivo* exploration due to their efficacy demonstrated in *in vitro* biological investigations. Every group possessed three identical rats. The dorsal hair was promptly removed, and the skin surface was thoroughly cleansed. Subsequently, the animals were positioned laterally. A sterile biopsy punch with a diameter of 12 mm was used to produce a circular incision by removing two layers of dorsal skin, resulting in a full-thickness excisional wound. The rats were placed in a secure, soundproof chamber maintained at a temperature of 21 ± 1 °C and a relative humidity of 35 ± 1 %. The space was regulated using a 12 h light and 12 h dark cycle. The examination of wound healing at a macroscopic level was performed at 14 days following the procedure.

2.9.3. Histological analysis

For this, the tissue samples were collected from the treated rats and fixed with 3.7 % paraformaldehyde for 2 days. Subsequently, decalcification was carried out using 12 % ethylene diaminetetraacetic acid (EDTA) at a temperature of 4 °C. Subsequently, the tissue samples underwent a process of cleansing and dehydration using alcohol. The desiccated samples were encased in paraffin wax to create thin sections, which were then stained using hematoxylin and eosin (H&E) staining and Masson's trichrome (MT) staining. The images were captured using an optical microscope.

2.10. Statistical analysis

All presented data are expressed as the mean ± standard deviation (SD). The data underwent statistical analysis using OriginPro 2019b software, employing the Student's *t*-test and one-way analysis of variance (ANOVA). Statistical significance was indicated by *($p < 0.05$) and ** ($p < 0.01$), while cases lacking statistical significance were denoted as non-significance (n.s.)

3. Results and discussion

3.1. Characterization of ZnTA and glycol chitosan

Metal-polyphenol conjugates show great potential as bioinspired materials for biomedical applications (J. Kim et al., 2021). The morphology was investigated by SEM, EDS mapping, AFM, and FE-TEM, as demonstrated in Fig. 1(a-d). The SEM image of TA (**Fig. S1)** and the ZnTA complex shows the morphological changes. TA is round-shaped particles ranging from 10 μm to 50 μm, whereas the ZnTA complex shows an undetermined cluster of particles. In the TEM image of Fig. 1 (c) the ZnTA complex, a scrambled structure was observed, which agreed with the SEM morphology. A similar assembly was observed in a study by Huang et al. (Yue Huang et al., 2023). EDS was performed to analyze the percentage of zinc, carbon, and oxygen in the ZnTA complex. As revealed in Fig. 1(b), 3.37 % zinc, 49.85 % oxygen, and 46.78 % carbon atomic weight were recorded in the ZnTA complex, confirming the presence of zinc ions in the ZnTA complex. The merged image of the ZnTA complex EDS mapping and map spectrum is shown in **Figs. S2** and **S3,** respectively. The dimensions of the ZnTA complex were further determined using AFM measurements. Fig. 1(d) depicts the 2D and 3D AFM pictures of synthesized ZnTA nanoparticles. The picture provides a good visualization of the topological structure and dispersion of nanoparticles. The ZnTA particles were observed to be within a range of 100 nm and exhibited an irregular star form, as verified by the TEM image. Further, Fig. 1(e) FTIR spectra validated the molecular structure difference between the TA and zinc-conjugated TA. The pure tannic acid showed characteristic peaks at 1700 cm^{-1}, representing the stretching of C=O groups (Yuxiang Huang et al., 2020). The peaks at 1606, 1532, and 1445 cm^{-1} were also observed due to the aromatic C-C stretches (Osolnik et al., 2024). Benzene rings were present through 1174 and 1015 cm^{-1}, whereas the vibration of O-H bonds out-of-plane and in-plane was attributed to 1307 and 752 cm^{-1}, respectively. The characteristic peaks of TA at 1700, 1606, 1444, and 750 cm-1 were retained in the ZnTA complex (Rasheed et al., 2021). However, a slight shift in other peaks was observed. The O-H peaks were shifted to 1313 cm^{-1}, and the benzene peaks were shifted to 1182 and 1020 cm^{-1}, showing the changes in TA structure after zinc incorporation (Fu et al., 2023). The modification also shifted the hydroxyl peak from 3311 to 3328 cm^{-1}. Hence, the shift of TA peaks in the ZnTA complex reveals the conjugation of zinc to functional groups of TA. As shown in Fig. 1(f), the XRD pattern of TA shows broad peaks at 14.16° and 25.05°, indicating the amorphous morphology. After the modification with zinc chloride, the peak formation was observed at 9.88°, 20.11°, 28.87°, and 33.16°. The crystallinity index (%) for peaks of TA (25.05°) and ZnTA (27.87°) was calculated to be 86.79 % and 45.05 %, respectively. This change in the peaks and their intensities confirms that the ZnTA complex was synthesized successfully. XPS analysis investigated zinc decoration upon TA and identified the elements. Fig. 1(g-i) shows the wide scan spectrum of the TA and ZnTA and high-resolution spectra of C1s, O1s, and Zn 2p of ZnTA (Fig. 1(g-(ii-iv)). The presence of zinc peaks confirms the modification of TA. The high-resolution XPS spectra of Zn 2p reveal that the binding energy of Zn 2p was divided into 1044.28 eV and 1021.28 eV. The first peak is attributed to Zn 2p1/2, and the second peak is the

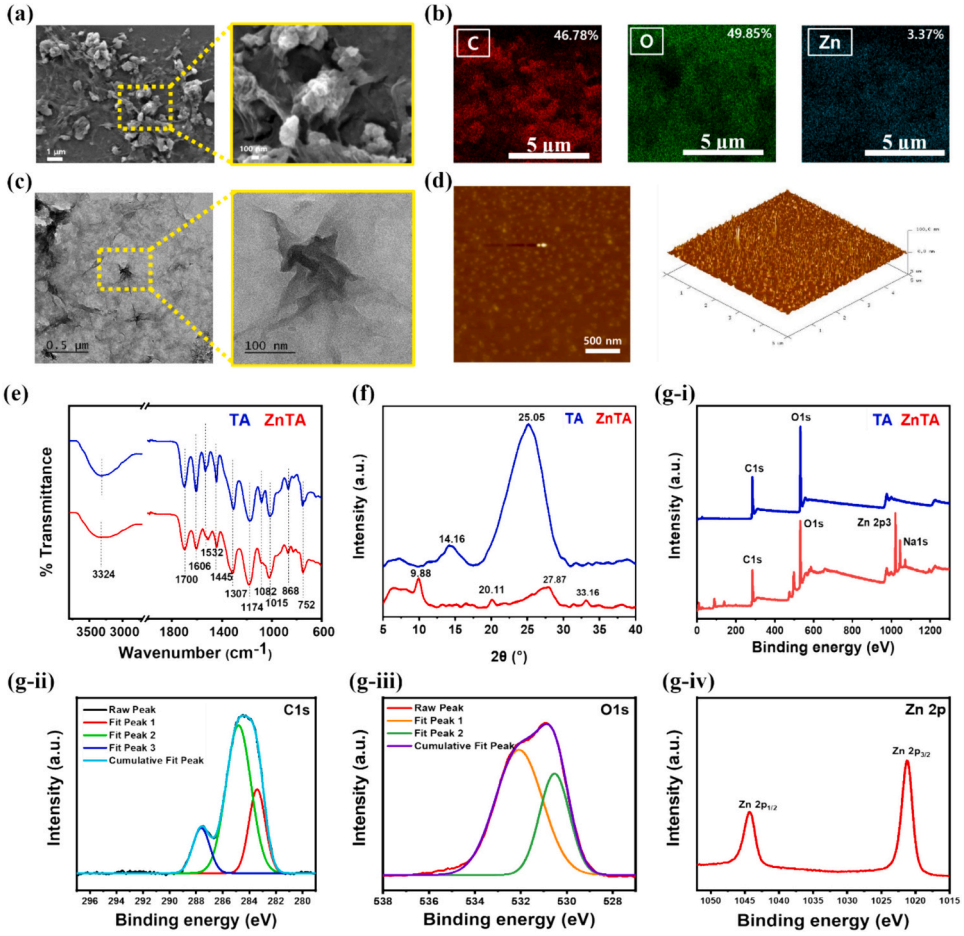

Fig. 1. Physicochemical properties of ZnTA complex (a) SEM, (b) Elemental mapping of ZnTA complex and atomic weight (%), (c) TEM, and (d) AFM shows the morphological structure of Zinc doped tannic acid (ZnTA), (e) FTIR spectra, (f) XRD spectra and (g-(i-iv)) XPS wide scan spectra of ZnTA and C1s, O1s and Zn2p core-level spectra.

resultant of Zn 2p3/2 respectively. The XPS of O1s deconvoluted into 2 peaks at 532.09 eV was attributed to zinc carbonate and C=O, whereas 530.53 eV was attributed to the zinc attached to the oxygen of tannic acid. Similarly, the 3 peaks appeared after the deconvolution of C1s of ZnTA. The peak at 287.6 eV is attributed to C=O, C-O, 284.8 eV is attributed to C=C, and 283.3 eV appeared due to C-C bonds present in TA. Hence, the overall outcomes of morphological and chemical characterizations show that the ZnTA particles were successfully synthesized.

Glycol chitosan was synthesized to increase its aqueous solubility and degradability. In the FTIR spectra demonstrated in Fig. 2(a), chitosan showed characteristic peaks at 3314 cm^{-1}, attributed to O-H and N-H stretching vibrations (Rodrigues et al., 2020). Other characteristic peaks such as 2925–2875 (C-H stretching), 1646 (C=O stretching of amide I), 1560 (N-H bending of amide II), and 1417 cm^{-1} (amide III) were also obtained. The presence of C-N, C-O-C, and C-O stretching was confirmed by peaks 1150, 1060, and 1025 cm^{-1}, respectively. After the modification to glycol chitosan, various peaks, including the amino group, hydroxyl group, and amide groups, were shifted. However, 1150 and 1060 cm^{-1} characteristic peaks were retained, showing the integrity of chitosan. The glycol-functionalized chitosan exhibited enhanced inter/intra-molecular –OH/NH peaks, indicating the successful grafting of the PEG chains with chitosan. Furthermore, significant enhancement in absorption intensity of –CH stretching (2878 cm^{-1}) also occurred in functionalized chitosan, contributed from the CH_2 moieties of the PEG chains. An additional absorption peak at 1466 cm^{-1} was observed in PEG-grafted chitosan, which can be attributed to the bending vibration of CH_2 groups of PEG chains (Andleeb et al., 2022). For further confirmation, ^{1}H NMR of chitosan and PEG-modified chitosan was performed, and the results are given in Fig. 2(b). The peak around $\delta =$ 2.04 and $\delta = 11.53$ is attributed to the deuterated acetic acid. However, the additional peak around $\delta = 3.7$ shows the PEG modification in the glycol chitosan. The proton peaks appearing between $\delta =$ 3.1–3.8 are attributed to different hydrogens in the CH_2 moieties, confirming the grafting of PEG chains with chitosan (Zaboon et al., 2019).

3.2. Morphological, structural, and thermal properties of scaffolds

The ZnTA complex was added to the gelatin/glycol chitosan solution to develop the multifunctional hydrogels *via* a simple and facile stirring process. The optimized parameters for all the hydrogels are mentioned in **Table S2**. After cross-linking and freeze-drying of scaffolds, samples were characterized. The images of the printed constructs are given in the inset of Fig. 3(a). The printed structures maintained their predesigned morphology, indicating their excellent printability. SEM images of the printed constructs at high and low magnification are presented in Fig. 3 (a). The bridges and junctions of the printed structure were visualized in the SEM images without further collapse, demonstrating the printed layers adequately adhered to each other through different interactions. ZnTA-incorporated scaffolds exhibited more porous morphological structures compared to the GC/ZT-0 scaffolds. The porous structure has several advantages in the biomedicine sector. The porous structures increase the surface area, facilitating cellular activity and antimicrobial activity through a smooth supply of nutrients and metabolic exchanges (Leng et al., 2021). It also facilitates the controlled release of bioactive elements, such as zinc ions, in a more methodical fashion, consequently

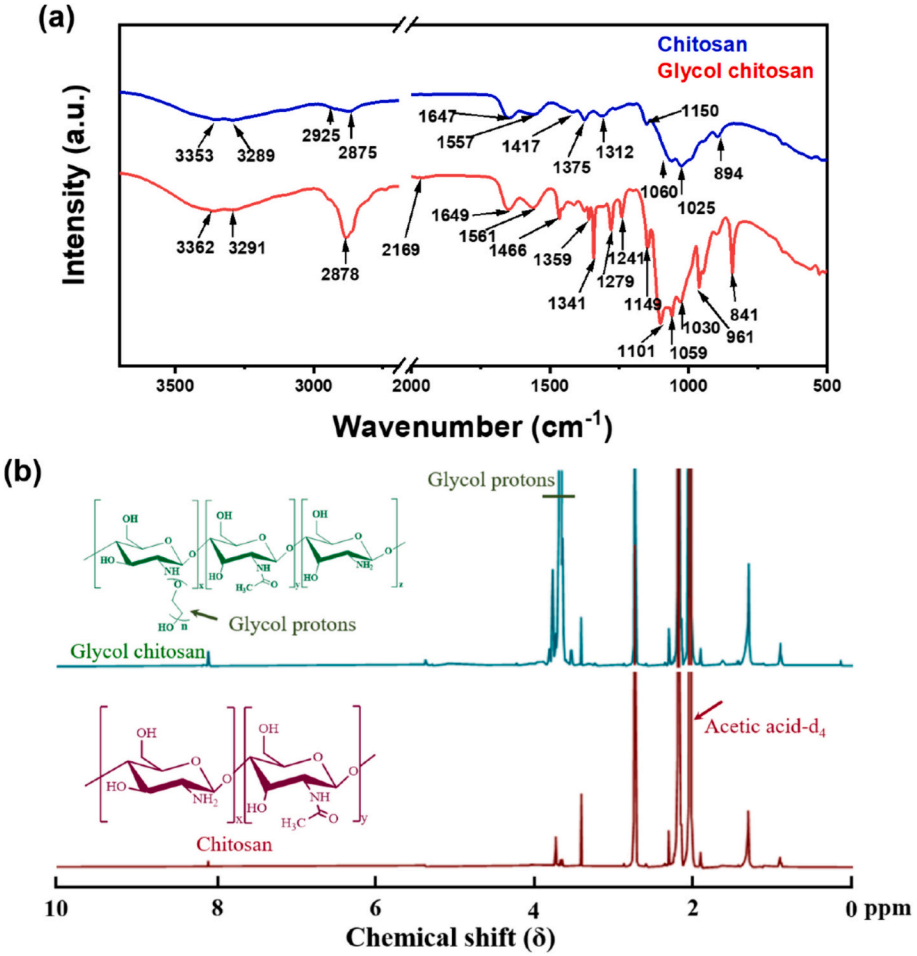

Fig. 2. (a) FTIR spectra, and (b) ^{1}H NMR spectra of chitosan and glycol modified chitosan.

enhancing the effectiveness of the treatment (Sutherland et al., 2023). Hence, the addition of the ZnTA complex to the hydrogels results in a porous structure, which improves their ability to fight against microorganisms and makes them suitable for many biomedical uses, including wound healing. The composition, temperature, concentration, and flow rate significantly impact the printing properties of hydrogels. A movie file during the hydrogel printing is given in Movie S1. The expansion ratio, uniformity factor, and integrity factor were computed to comprehend the printing characteristics of GC/ZT hydrogels. Fig. 3(b) presents the expansion ratio of hydrogels at a specific temperature. The expansion ratio of hydrogel should approximate unity. Based on the concentration of the ZnTA complex, the findings suggest that the expansion ratio of the printed scaffolds exhibited variability. The GC/ZT-4 hydrogel maintained the diameter in close proximity to the needle diameter. It exhibited favorable mechanical strength, physical bonding, and chemical coordination, ensuring the hydrogel's integrity was effectively preserved. Fig. 3(c) and (d) provide the manufactured hydrogels' integrity and uniformity factors, respectively. The findings suggest that the concentration of the ZnTA complex significantly impacts both the length of the strand and the thickness of printed structures. Based on the comprehensive analysis of various parameters, it is evident that the GC/ZT-4 hydrogels exhibited favorable printing properties.

The FTIR spectra of GC/ZT-0, GC/ZT-1, GC/ZT-2, and GC/ZT-4 are presented in Fig. 3(e). Typical peaks of glycol chitosan were shown at 3291 cm^{-1} (OH stretching vibration), 1631 cm^{-1} (C=O stretching vibration), 1535 cm^{-1} (N-H bending vibration), 1447 cm^{-1} (symmetric stretching of –COOH groups) and 1077 cm^{-1} (C-O stretching vibration). The gelatin/glycol chitosan composite exhibited a peak corresponding to gelatin at 1631 cm^{-1} and 1406 cm^{-1} (symmetric stretching of $–COO^-$ groups), indicating that glycol chitosan was evenly blended with gelatin. This interaction could arise from the electrostatic interaction between the ammonium ($-NH_3^+$) ions of chitosan and the carboxyl ($–COO^-$) ions of gelatin, a partial transformation of electrostatic bonds into chemical bonds through hydrogen bonding. The XRD analysis was performed to examine the effects of the added ZnTA, and the patterns are depicted in

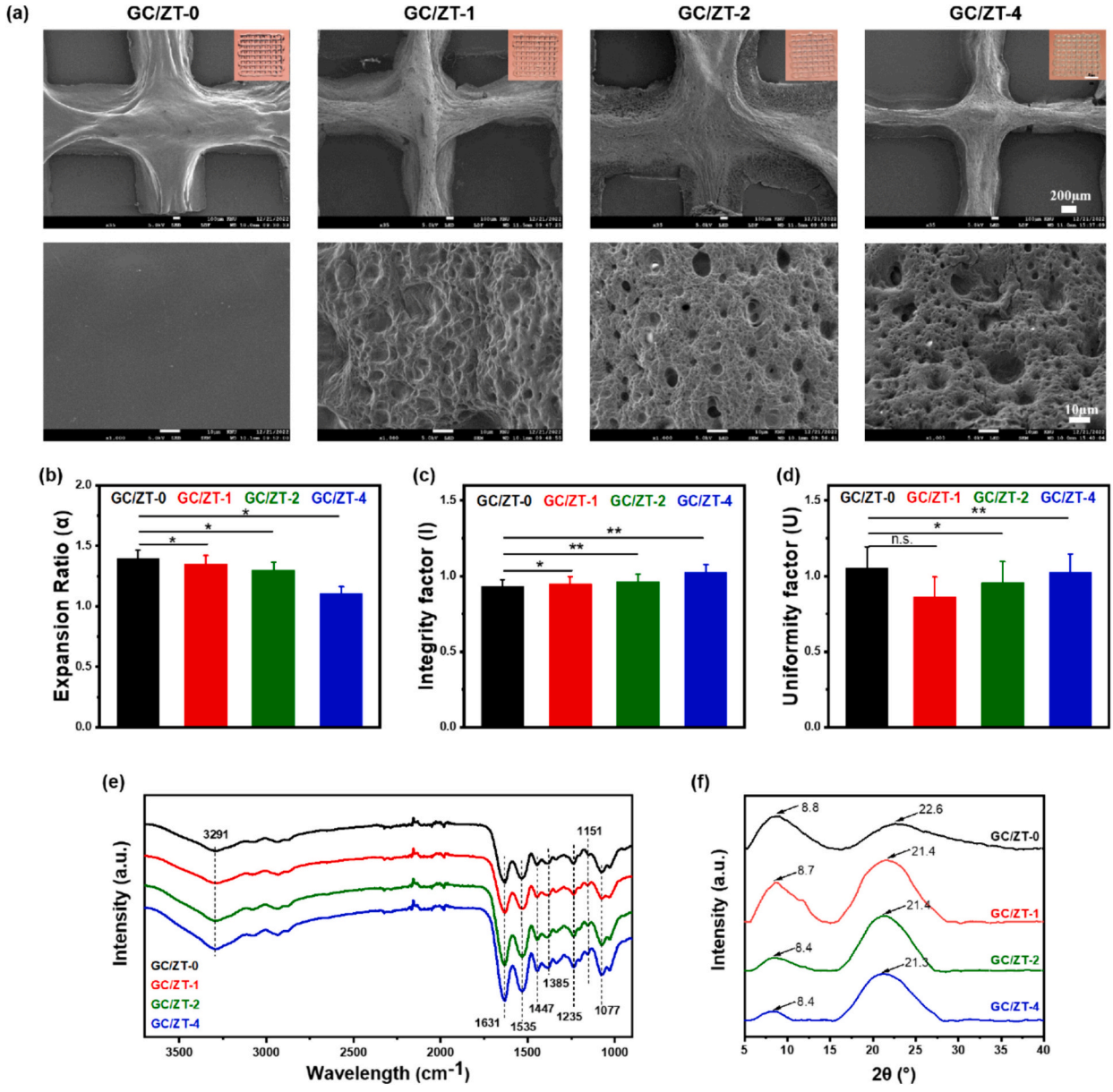

Fig. 3. Characterization of GC/ZT scaffolds (a) Photographic (after printing) images and SEM images of 3D-printed freeze-dried scaffolds (low and high magnification), (b) Expansion ratio, (c) Integrity factor, and (d) Uniformity factor of developed GC/ZT hydrogels, (e) FTIR and (f) XRD of fabricated scaffolds.

Fig. 3(f). The pure polymer (GC/ZT-0) shows two broad diffraction peaks at 8.8° and 22.8° with interlayer distances of 1.013 and 0.39 nm, respectively. These peaks are attributed to glycol chitosan and triple-helical collagen structure in gelatin (Kim et al., 2024; Lu et al., 2022). These peaks were significantly shifted towards lower diffraction angles of 8.4° and 21.3° in the ZnTA-added composite with interlayer distances of 1.056, and 0.42 nm, respectively. The enhanced interlayered distances can be attributed to the insertion of ZnTA complex inside the polymer galleries, facilitating interactions between ZnTA and polymer chains (Nagahama et al., 2009). These FTIR and XRD results revealed that the ZnTA was successfully incorporated in a gelatin/glycol chitosan polymer mixture.

The TGA was performed to analyze the thermal stability of GC/ZT scaffolds. TGA and DTG curves in **Fig. S4**(a, b) depict the thermal degradation behavior of GC/ZT scaffolds. All scaffolds predominantly exhibited two steps of thermal degradation. The lower degradation regions (<200 °C) can be attributed to the loss of the bound water molecules. The major degradation occurred at >300 °C due to the decomposition of ionic bonds and amine groups in the polymeric chains present in the scaffolds. The weight loss was slightly higher in ZnTA-added scaffolds compared to pure polymers due to the presence of more heat-sensitive groups in the composite scaffolds (Horn et al., 2009). These degradation patterns were also observed in the DTG curve, where the major peak occurred >300 °C, showing the major weight loss (Fernandes et al., 2011).

3.3. Wettability and degradation analysis

Contact angle measurements were employed to prove the difference in wettability properties of GC/ZT films before and after the incorporation of ZnTA particles. As illustrated in Fig. 4(a, b), the contact angle of GC/ZT-0 is 54.2° ± 0.83. As the ZnTA is added and the concentration increases, the contact angle of the films increases from 71.48° ± 0.76, 74.31° ± 0.65 to 116° ± 0.88. The increase in contact angle was undoubtedly due to the presence of ZnTA particles (Patil et al., 2021). These hydrophilic scaffolds can improve cell adhesion and proliferation (Ehtesabi & Massah, 2021). Therefore, based on the above results, the GC/ZT films had good wettability except for the GC/ZT-4 films. These results also evidenced that adding the ZnTA complex successfully modified gelatin/glycol chitosan properties.

The degrading characteristics of the scaffolds were examined in 1× PBS solution at room temperature, and the results are shown in Fig. 4(c). An appropriate degradation rate is required for improved cellular activity. Rapid degradation or slow degradation is not ideal for tissue

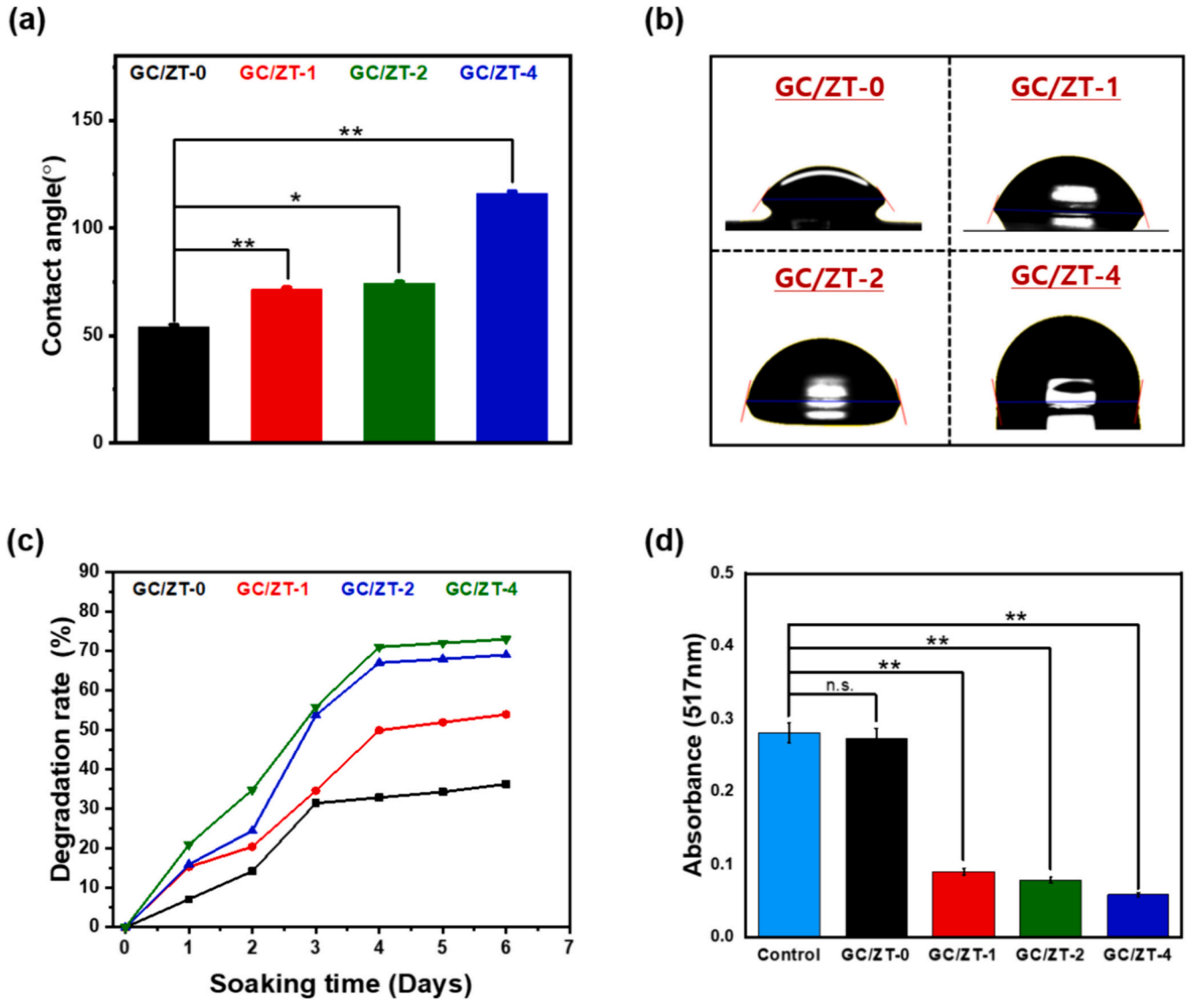

Fig. 4. (a) Quantitative results and (b) Images of GC/ZT film contact angle (c) Degradation rate of scaffolds in 1× PBS and (d) DPPH scavenging activity of scaffolds.

engineering applications (Tondera et al., 2016). The composite scaffolds showed faster degradation compared to the pure polymer scaffolds, which can be attributed to the high porosity of the scaffolds, which facilitates rapid movement of the solvent molecules, leading to faster degradation.

3.4. Antioxidant properties and zinc release

An infected wound can generate excessive free radicals, which cause oxidative stress. This causes DNA damage, endothelial dysfunction, enzyme degradation, tissue injury, and lipid peroxidation (Mittal et al., 2014; Sharifi-Rad et al., 2020). Scaffolds with antioxidant potential can effectively scavenge free radicals, which is helpful for chronic wound healing. Polyphenols such as gallic and tannic acids possess good antioxidant potential (Lou et al., 2018). The DPPH radical-scavenging potential was evaluated with and without scaffolds. Fig. 4(d) shows the radical scavenging activity after 2 h, and **Fig. S5** shows activity at various time intervals. The improved activity was basically due to the presence of tannic acid in the ZnTA complex (Leite et al., 2021). Therefore, the hydrogel has effective potential in wound repair due to its radical scavenging activity.

The release profile of zinc ions was examined by soaking the samples in 1× PBS solution for varying times. The results presented in **Fig. S6** show that zinc ions were released before the full degradation of scaffolds. The composite scaffolds exhibited rapid release vis-à-vis pure polymer scaffolds due to their porous structure, which facilitated the movement of solvent molecules and accelerated faster release.

3.5. Rheological analysis

The viscoelasticity of the hydrogels plays crucial roles in 3D-printing for the desired applications (Ning et al., 2020). The linear viscoelastic (LVE) region was determined through the strain amplitude sweep, and the results are presented in Fig. 5(a). The hydrogels maintained their structural integrity up to 10 % of shear strain, showing the existence of compact networks. The hydrogels showed improved storage modulus vis-à-vis storage modulus, indicating their elastic properties. The frequency sweep was performed to monitor the effects of the added material on the storage modulus (G′) and loss modulus (G″) of the hydrogels, and the results are given in Fig. 5(b). The composite hydrogels showed improved G′ (continue lines) compared to the pure polymer hydrogels, attributing the presence of cross-linked polymeric networks. This was further increased with increasing ZnTA contents due to the greater availability of reactive functional groups for interactions, including hydrogen bonding, cationic-π interactions, and π-π interactions (Lee, 2018). The value of G″ was lower than G′ throughout the measured regions, showing the elastic characteristics of the hydrogels. The composite hydrogels demonstrated enhanced G″ values compared to the pure polymer hydrogels but were lower than G′, showing superior viscoelastic properties. The corresponding change in viscosity complex (η*) throughout the measured regions is given in Fig. 5(c). The composite hydrogels demonstrated enhanced η* compared to the pure polymer hydrogels. This can be attributed to the presence of more cross-linked network structures in the hydrogels, restricting the motion of the polymer chains in given conditions. The change in viscosity of the hydrogels at different temperatures (25–50 °C) is given in **Fig. S7**. The composite hydrogels showed improved viscosity than the pure polymer hydrogels throughout the measured regions, indicating more cross-linked structures in the hydrogels. The dramatic decreased in viscosity was observed above 30 °C, showing the transition of the gel state into the sol-state due to the disentanglement of the polymeric chains. Thixotropic measurements were conducted to evaluate the hydrogel's recovery capacity after deformation, and the results are shown in Fig. 5 (d).

The G′ value of the hydrogels was gauged at distinct shear rates: 1.0 %, 100 %, and 1.0 % at a temperature of 25 °C. A considerably high shear rate (100 %) induced deformation in the hydrogel, reducing its viscosity. Upon the end of the shear rate, the hydrogels restored their

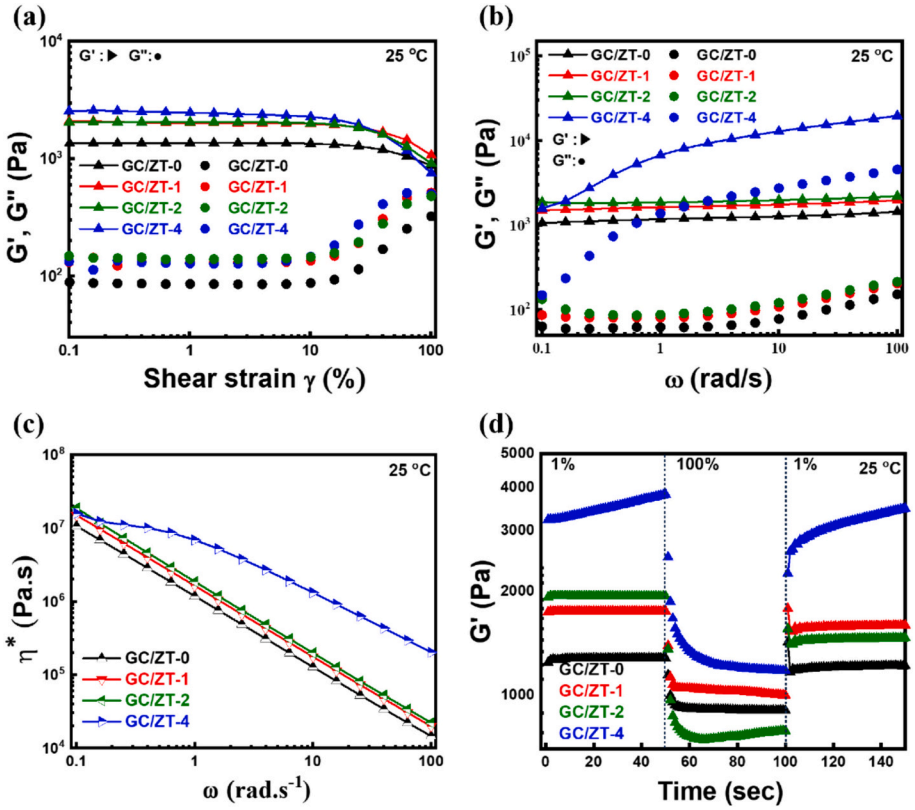

Fig. 5. Rheological properties of hydrogels: (a) Amplitude sweep, (b) Oscillation frequency sweep, (c) Viscosity complex, and (d) Thixotropic behavior of hydrogel.

initial viscosity. Initially at 1 %, G′ value was 1281, 1752, 1939, and 3821 Pa for GC/ZT-0, GC/ZT-1, GC/ZT-2, and GC/ZT-4, respectively. After removing high shear rate (100 %), hydrogels approximately regained its initial G′ value. The regained G′ value was 1233, 1468, 1588, and 3474 Pa, for GC/ZT-0, GC/ZT-1, GC/ZT-2, and GC/ZT-4, respectively. The higher recovery property in the composite hydrogels was attributed to the establishment of crosslinked structures fostered by more robust interactions, including, hydrogen bonding, cationic-π interactions, and π-π interactions within the hydrogel following the termination of shear. Consequently, the admirable recovery characteristic of the composite hydrogels devised in this investigation underscores their promising potential as a novel self-healing hydrogel.

3.6. Adhesive property

The adhesive hydrogel dressing exhibits multifunctional attributes, encompassing wound adherence, closure, antibacterial protection, bodily fluid containment, and hemostasis facilitation. The adhesive efficacy of the GC/ZT hydrogels was evaluated through shear lap stress testing, as depicted in the schematic of Fig. 6(a). GC/ZT hydrogel promptly exhibited adherence to a range of materials, encompassing biological tissues (skin) as well as plastic, glass, rubber, and metal (Fig. 6 (b)). UTM measured the quantitative results, as shown in Fig. 6(c, d), to plot load and adhesive strength *vs.* displacement curves for all hydrogels. The adhesive strength of hydrogels was significantly enhanced, ranging from 150 to 210 kPa with an increasing content of ZnTA. The ultimate adhesive strength of hydrogels is presented in Fig. 6(e). The GC/ZT-4 hydrogel demonstrated enhanced load-bearing properties compared to GC/ZT-0 due to stronger interactions of active functional groups of hydrogel bonding with externally applied surfaces. The adhesive performance of the GC/ZT-4 hydrogel was also tested against porcine skin through lap shear testing. The results are shown in **Fig. S8**. The hydrogel has satisfactory adhesive properties on porcine skin compared to other materials examined. Prior studies have demonstrated that the adhesion strength of hydrogels is intricately tied to the cohesion within the hydrogel itself and the adhesive interaction at the interface (Bu & Pandit, 2022; Zhang et al., 2020). Concerning the GC/ZT hydrogel system, an elevated proportion of ZnTA creates sensitive quantities of polyphenol groups and zinc ions, simultaneously supplementing crosslinking density. This synergistically reinforces the interfacial adhesion and internal cohesion of the hydrogels. It can be suggested that the robust finger adhesiveness observed in GC/ZT hydrogels primarily arises from the polyphenol, hydroxyl, and amino groups of the hydrogel structure. These constituents exhibit substantial affinity for the charged functional groups on the skin surface, encompassing thiol and amine groups found in polypeptides and proteins (Chen et al., 2022; Wang et al., 2020). Hydrogels containing numerous hydroxyl moieties might interact significantly with charged functional groups of human skin peptide chains *via* hydrogen bonding, electrostatic interactions, ion-dipole, and dipole-dipole bonds to promote adhesiveness (Bal-Ozturk et al., 2021). These GC/ZT hydrogels have good adhesion capability, which enables them to adhere strongly to the surrounding tissues, prevent subsequent cracking, and offer a physical barrier to terminate bleeding.

3.7. Antibacterial and antibiofilm properties

Bacteria can easily grow in open and fresh wounds, making them critical to cure. Therefore, an ideal wound dressing should possess strong antibacterial properties to inhibit and eliminate the growth of bacteria. The bacteria-killing effects of developed hydrogels were examined against *B. subtilis* and *E. coli* bacteria after 12 h of incubation

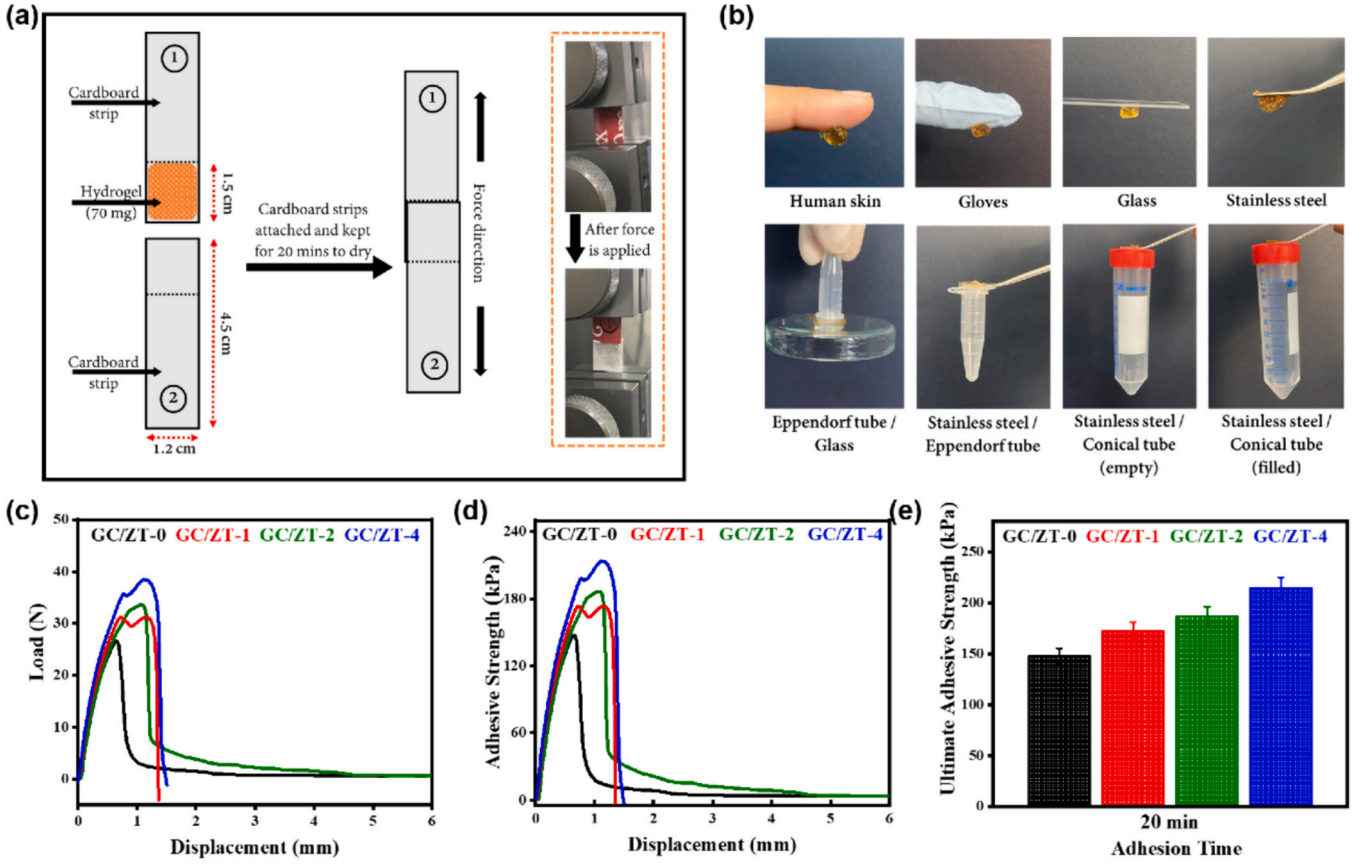

Fig. 6. Adhesive properties of GC/ZT hydrogels: (a) Adhesion of hydrogel to various natural and synthetic platforms, (b) Schematic presentation of lap-shear test performed, (c) Load-displacement curves, (d) Adhesive strength, and (e) Ultimate adhesive strength of GC/ZT hydrogels.

and the results presented in Fig. 7(a, b). All scaffolds showed outstanding antibacterial properties. The bacteria-killing efficiency was calculated based on the optical density of the bacteria culture after the treatment. The antibacterial efficiency of GC/ZT-0 scaffolds was >81 % against *B. subtilis* and 92.7 % against *E. coli,* which was confirmed by the agar plate diffusion method (Fig. 7(d). The antibacterial potential of ZnTA-added scaffolds was maintained in gram-positive bacteria but decreased in gram-negative bacteria. As reported previously, gelatin is impotent for killing bacteria (Shankar et al., 2016). Therefore, the antibacterial activity observed in GC/ZT-0 is the predominant effect of glycol chitosan. The activity is slightly reduced in GC/ZT-1, 2, and 4 compared to the GC/ZT-0 sample. However, compared to the control,

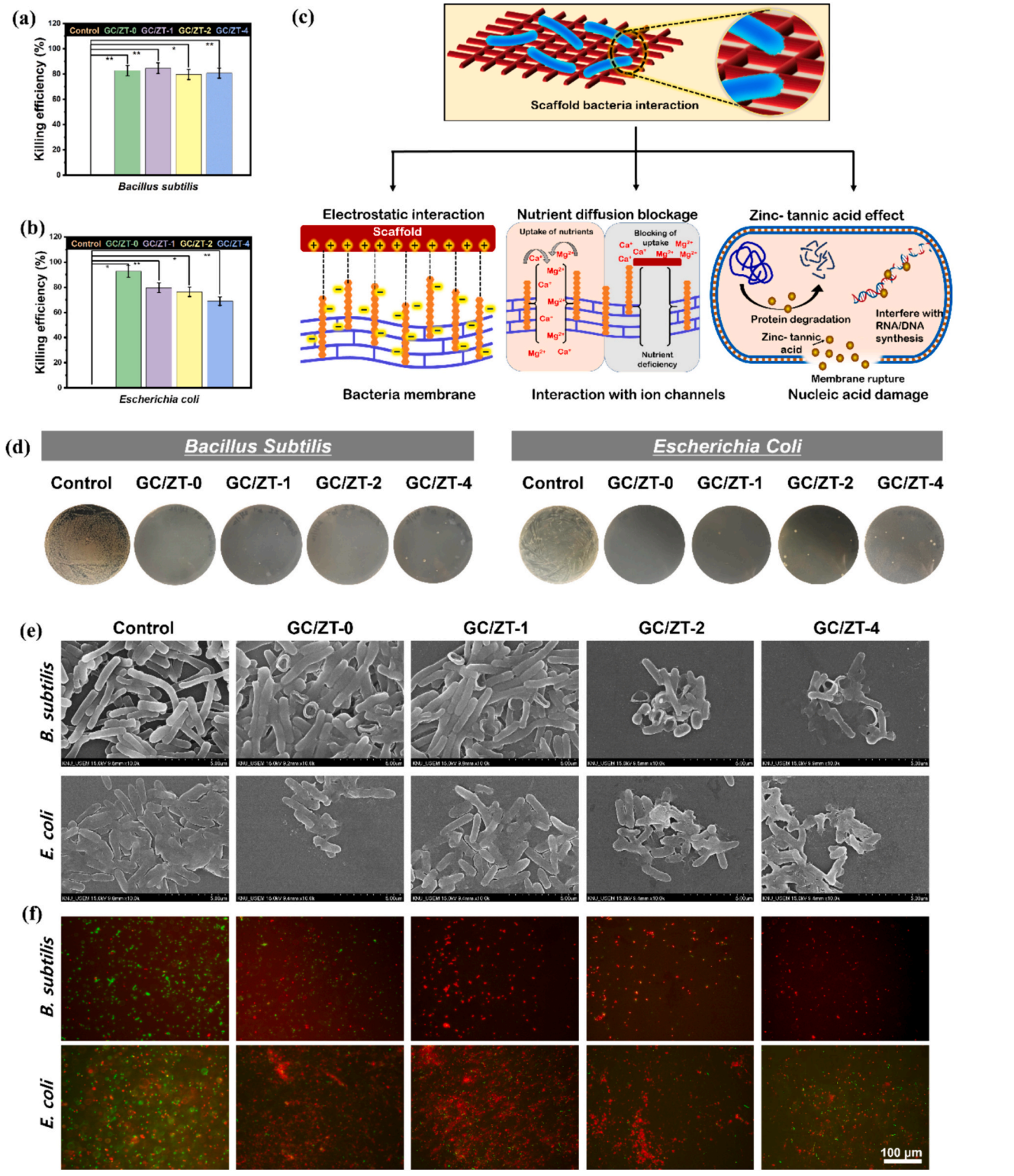

Fig. 7. Antibacterial properties of GC/ZT scaffolds (a, b) Percent inhibition of *B. subtilis* and *E. coli* (c) Schematic representation of possible interactions of scaffold with bacteria to inhibit the bacterial growth and eradicate in presence of GC/ZT treatment, (d) Agar plating of scaffold treated bacteria, (e) SEM images and (f) Live/dead assay of bacteria cultures with GC/ZT scaffolds.

which received no treatment, the antibacterial potential of all hydrogels showed outstanding results, primarily due to the presence of ZnTA particles and glycol chitosan. Fig. 7(c) shows the possible mechanisms for the bactericidal effect of GC/ZT scaffolds. Zinc ions damaged the bacterial cell membrane and inhibited the growth of bacteria by interfering with replication and metabolism (Almoudi et al., 2018; Sathishkumar et al., 2022). TA is a polyphenol that exhibits bactericidal properties by disrupting cell membranes, inhibiting bacterial enzymes, and maintaining protein integrity (Farha et al., 2020). Chitosan can damage bacteria by binding to negatively charged cell walls, disrupting them, and releasing the internal components. It can also interfere with DNA replication and inhibit the multiplication of bacteria (Yilmaz Atay, 2020). Hence, the developed GC/ZT scaffold synergistically enhances the bactericidal properties through various mechanisms. The antibacterial results were confirmed by SEM image analysis, as demonstrated in Fig. 6(e). More damaged bacteria membranes occurred in scaffold-treated groups compared to the control, showing their superior antibacterial potential. The live/dead analysis showed a higher number of live bacteria (green stain) in the control group and dead bacteria (red stain) in the treatment groups, as given in Fig. 7(f).

Further, a biofilm inhibition test of GC/ZT scaffolds was conducted to understand the effectiveness of these scaffolds against *B. subtilis* and *E. coli*, and the results are shown in Fig. 8(a). Biofilm protects the bacteria against external factors and keep them safe, which is dangerous for chronic wounds. Therefore, the disruption of biofilm is necessary for effective wound healing. The dark stain of crystal violet is visible for the control set of bacteria. However, the treatment sample shows a significant reduction in the stain. The scaffolds-treated groups effectively disrupted the biofilms, showing their antibiofilm property. The absorbance value of the treated groups is given in Fig. 8(b, c). These results indicate that GC/ZT samples could effectively disrupt biofilm formation, mainly by killing bacteria and entering the microenvironment to disturb the biofilm intimacy.

3.8. Biocompatibility, cell migration, and in vitro examination

The biocompatibility of samples is an important and mandatory property for application in tissue engineering. The biocompatibility and cell proliferation of GC/ZT scaffolds were evaluated by the WST-8 assay, and outcomes are shown in Fig. 9(a, b). The cells (HDF, macrophages) cultured without any sample were considered a control group. All samples were identified as nontoxic to fibroblast cells and macrophages, as, after all treatments, cells had over 80 % viability, confirming that the GC/ZT samples are highly biocompatible with HDF cells and macrophages. The GC/ZT-4 showed outstanding growth in the cell count, which shows that the polymer and ZnTA incorporation were encouraging the growth of cells.

The impact of GC/ZT sample leachates on promoting cell migration was investigated by a scratch test. According to Fig. 9(d), the GC/ZT-4 hydrogel significantly improved the migration of HDF cells. It resulted in the closure of the scratch in comparison to the control, GC/ZT-0, GC/ZT-1, and GC/ZT-2. The cell migration seen in the GC/ZT-0 group indicated that the polymer matrix can facilitate HDF cell movement. The numerical outcomes of cell migration are presented in Fig. 9(c). Furthermore, the movement of cells in other groups was affected by the presence of the ZnTA complex. The group that contained 4 % ZnTA exhibited increased migration, indicating that the ZnTA compound increases cell mobility. Therefore, the GC/ZT hydrogels can enhance the movement of HDF cells, which is a crucial characteristic for expediting the healing process of wounds.

Further, the influence of the sample on HDF cell growth and proliferation through the modulation of cell cycle regulatory genes and wound healing genes was thoroughly investigated. Fig. 10(a) presents a schematic representation of the upregulated genes with scaffolds. The enhanced proliferative efficacy of GC/ZT-4 is attributed to the synergistic combination of ZnTA and gelatin/glycol chitosan. The quantitative expression of cell cycle regulatory genes (*PCNA*, *CDK4*, *CDK6*) and wound healing genes (*Fibronectin*, *Collagen*, and *TGF-β1*) was conducted following treatment with GC/ZT hydrogels. Significantly divergent expression levels were observed across all genes. Proliferating cell nuclear antigen (*PCNA*), crucial for nucleic acid metabolism and cell proliferation, along with *CDK4* and *CDK6*, pivotal in cell division progression, exhibited notable upregulation, as depicted in Fig. 10(b–d). Specifically, the fold change in *PCNA*, *CDK4*, and *CDK6* gene expression for GC/ZT-4 treated samples was 49.5, 2.3, and 76.3 on day 1, respectively. Surprisingly, on day 7, *PCNA* and *CDK6* showed fold changes of 3.4 and 6.2, respectively, while *CDK4* increased to 2.9. These upregulated values indicate a significant increase in proliferating cells within

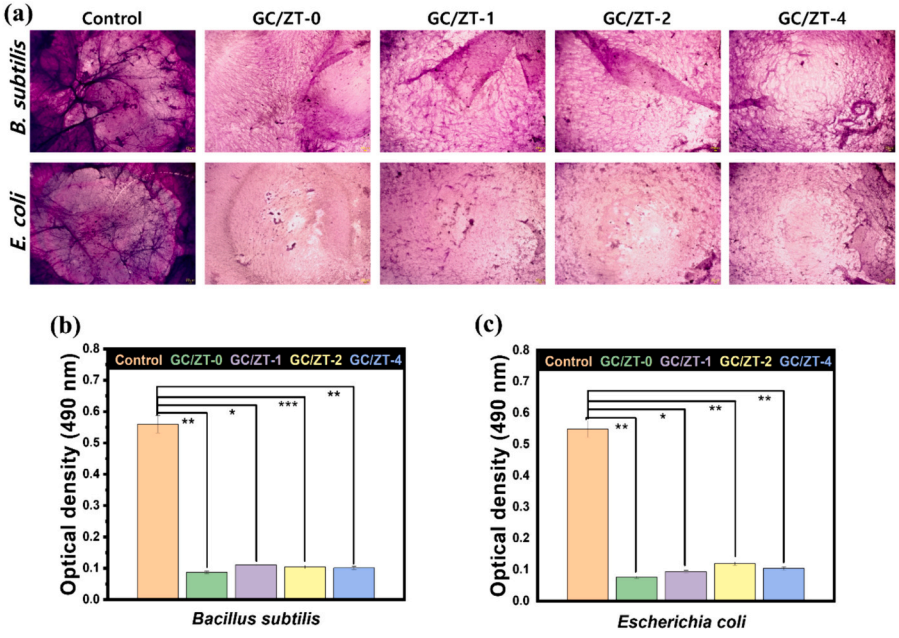

Fig. 8. Antibiofilm effect of GC/ZT scaffolds (a) Microscopy images of sample-treated *B. subtilis* and *E. coli* biofilms after crystal violet staining and (b, c) Absorbance at 490 nm.

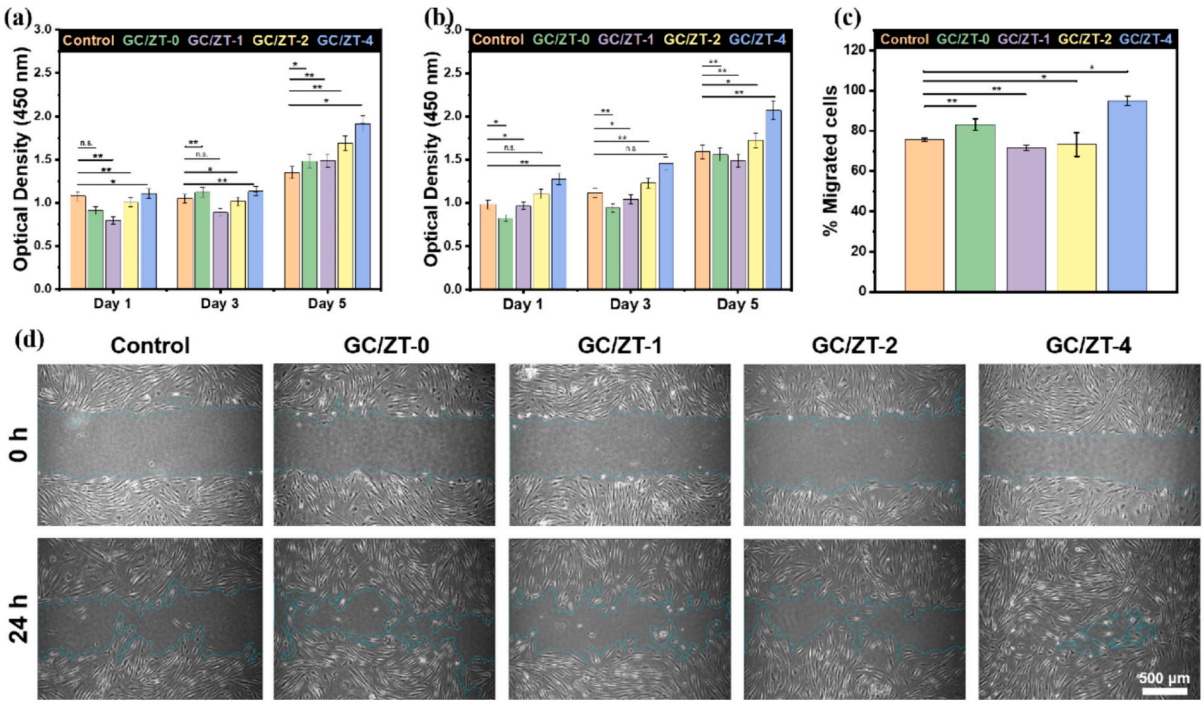

Fig. 9. (a) Cell viability of HDF cells, (b) Cell viability of macrophages, and (c) Quantitative results and (d) Their respective images of HDF cells migration.

the GC/ZT-4 treatment group.

Moreover, wound healing genes were analyzed to discern their expression in the presence of GC/ZT samples on HDF cells, as illustrated in Fig. 10(e–g). The results revealed high expression levels of *Fibronectin*, *Collagen*, and *TGF-β1* in HDF cells treated with the sample, both after 1 and 7 days of culture. *TGF-β1*, a multifunctional cytokine, is implicated in myofibroblast trans-differentiation. Notably, the fold change for *TGF-β1* on day 1 ranged from 0.017 to 4.62 for GC/ZT-0 to 4 samples, with a subsequent increase by day 7. The expression was significantly upregulated in GC/ZT-2 and GC/ZT-4 hydrogels, with fold changes of 2.18 and 15.22, respectively. The gene expression of *Collagen* and *Fibronectin* after 1 and 7 days of treatment is depicted in Fig. 10(f, g). *Fibronectin* and *Collagen* play crucial roles in wound healing by promoting fibrous network formation and serving as the primary structural components of connective tissue, respectively (Arif et al., 2021; Kendall & Feghali-Bostwick, 2014). The scaffolds treated groups exhibited enhanced expression of the wound healing genes compared to the control. This was significantly higher in ZnTA-added scaffolds. The enhanced expression of *TGF-β1*, *Fibronectin* and *Collagen* in scaffolds treated groups was attributed to the synergistic effects of the added materials, including zinc, tannic acid, gelatin and glycol chitosan. These materials play significant roles in wound healing by regulating different physiological functions, including antibody production, lymphocytes, blood clotting, collagen synthesis, boosting immunity, and antimicrobial activity (Jennifer Sallit, 2012). Zinc ions play crucial roles in collagen synthesis, immunity boosting as well as inflammation (Yang et al., 2022). Tannic acid has anti-inflammatory characteristics and maintained moisture equilibrium in the wound area, which is essential for promoting efficient healing. The glycol modified chitosan showed enhanced cellular and microbial activities, as well as collagen synthesis, accelerating the generation of new tissues (Divyashri et al., 2022; Moeini et al., 2020). Gelatin trigger the collagen formation, and cellular activity, providing suitable platform for wound healing (Cao et al., 2024; Kang & Park, 2021). Thus, developing the 3D-printed constructs based on these materials have huge advantages in biomedical sectors. To validate the findings from qRT-PCR, the protein expression levels of *Fibronectin* and *Collagen* were assessed. As illustrated in Fig. 10(h), *Fibronectin* intensities notably increased in the GC/ZT-2 and GC/ZT-4 treatment groups following the qRT-PCR results. Similarly, GC/ZT-4 demonstrated a significant impact on HDF cells, resulting in prominent *Collagen* expression. These outcomes validate the upregulation of wound healing-related genes.

3.9. *In vitro* effect on macrophage polarization

Macrophage polarization is crucial in wound healing, influencing infection prevention, cell growth promotion, inflammation reduction, and tissue modification. Depending on the microenvironment, macrophages can adopt M1 or M2 phenotypes (Dutta et al., 2023). For instance, M1 macrophages secrete *Interleukin-1* (*IL-1*) and other pro-inflammatory cytokines, triggering an inflammatory response in bacteria-infected wounds. Conversely, M2 macrophages express *Interleukin-10* (*IL-10*) and *Arginases-1* (*ARG-1*), fostering anti-inflammatory responses and promoting cell migration, proliferation, and skin regeneration (Joorabloo & Liu, 2022).

To assess the modulation of GC/ZT hydrogels on macrophage polarization, we conducted a comprehensive investigation employing optical imaging, qRT-PCR, and ICC. Optical images revealed distinct morphological changes in macrophages treated with GC/ZT hydrogels. Previous studies have established that macrophage polarization can be distinguished based on morphological characteristics. Specifically, elongated morphology typically corresponds to M2 polarization, while round-shaped morphology indicates M1 polarization, as elucidated in previous research (Dutta et al., 2023). As Fig. 11(a) illustrates, macrophages treated with GC/ZT-0 exhibited a round-shaped morphology, whereas samples incorporating ZnTA displayed a more elongated morphology. qRT-PCR analysis further elucidated the molecular mechanisms underlying macrophage polarization. qRT-PCR was conducted for the M1 (*IL-6*) and M2 (*IL-4*, *ARG-1*, *VEGF*, *CD163*, and *IL-10*) genes. *IL-6* plays a role in switching macrophage polarization from the M1 phenotype to M2. Notably, the expression of *IL-6* (Fig. 11(b)), known for its role in M1 to M2 phenotype switching, was significantly elevated in GC/ZT-treated groups, suggesting a shift towards M2 polarization (Liu et al., 2022). The gene expression of M2 macrophages was analyzed using *IL-4*, *ARG-1*, *VEGF*, *CD163*, and *IL-10* marker genes. GC/ZT sample groups significantly elevated the expression of *IL-4*, *CD163*, and *IL-10*

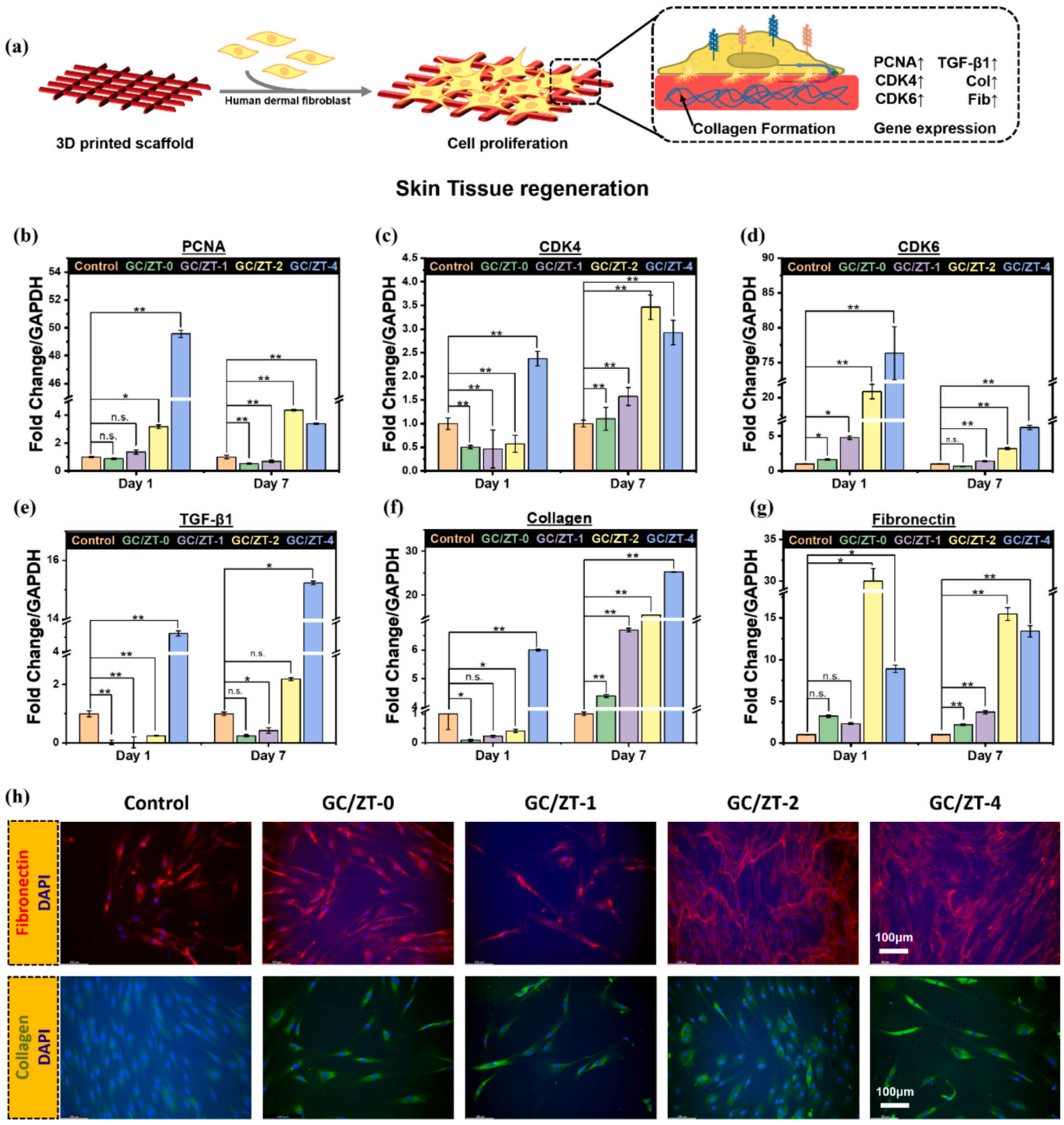

Fig. 10. (a) Schematic presentation for expression of genes in presence of samples, (b-g) qRT-PCR results of *PCNA*, *CDK4*, *CDK6*, *TGF-β1*, *Fibronectin*, and *Collagen* after the treatment of day 1 and day 7, (h) ICC images of HDF cells after treatment of 5 days (red: *fibronectin*; green: *collagen*; blue: nucleus).

compared to the control groups. Upregulation of *ARG-1* and *VEGF* genes compared to control was improved only in GC/ZT-4 treated groups. All other hydrogels down-regulated the expression of *ARG-1* and *VEGF*. Fig. 11(b) shows that gelatin/glycol chitosan could highly promote M1 polarization over M2. So, it is clear that the ZnTA complex is responsible for the M2 polarization of macrophages. To confirm the above results, immunocytochemistry of control and GC/ZT-4 was performed for protein expression of M1 (*CD68*) and M2 (*CD163*, *CD83*) markers. The ICC corroborated these findings, highlighting the enhanced polarization of M2 macrophages in GC/ZT-4-treated samples. As Fig. 11(c) demonstrated, the GC/ZT-4 group displayed remarkably higher CD163 and CD83 levels than the control group. Overall, our results indicate that GC/ZT hydrogels, especially GC/ZT-4 with a high concentration of ZnTA, effectively promote M2 macrophage polarization, facilitating tissue regeneration. These findings underscore the potential of GC/ZT hydrogels as promising candidates for applications in wound healing therapies, warranting further investigation into their practical utility.

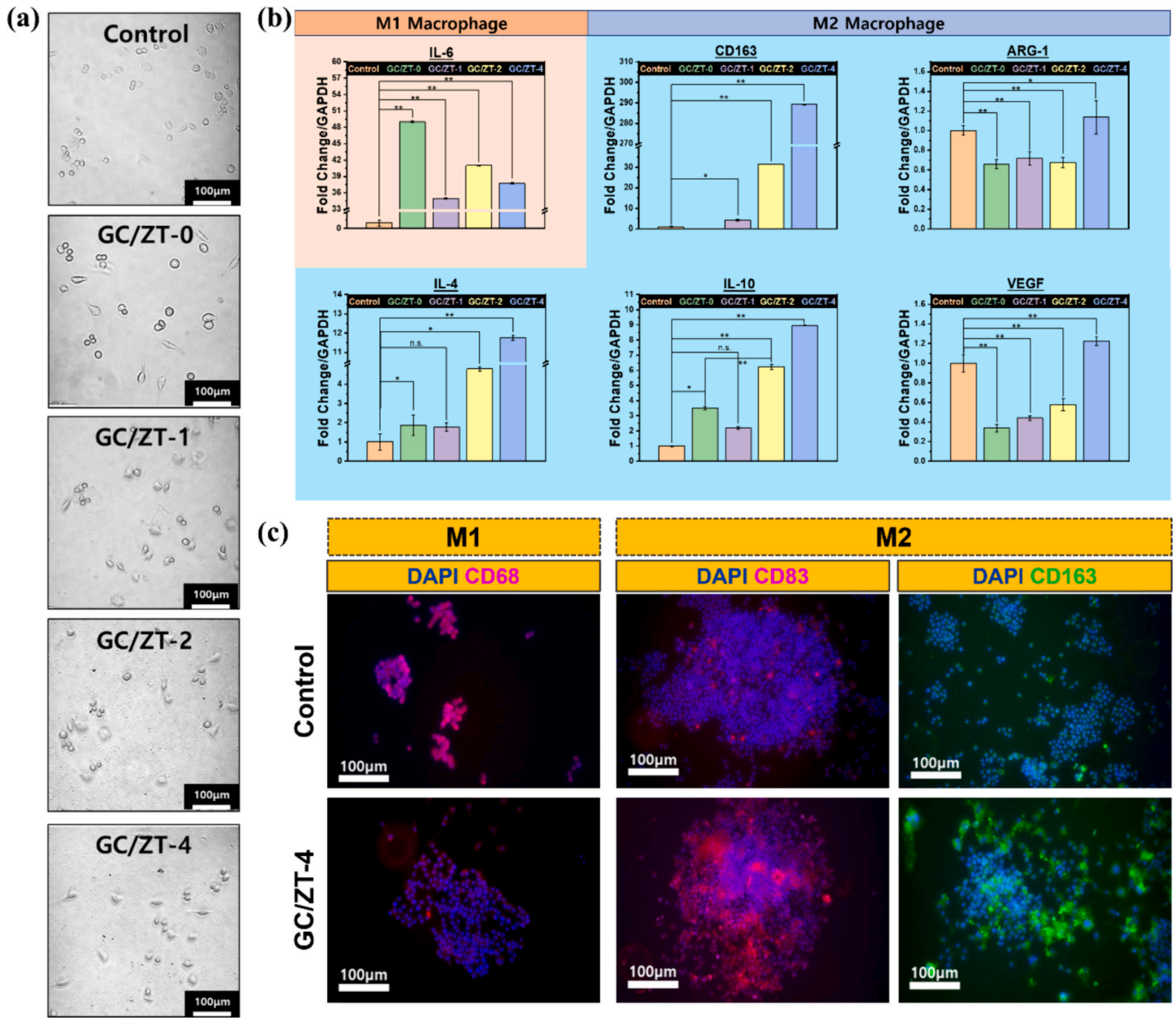

Fig. 11. (a) Optical images of macrophage after treatment (b) qRT-PCR results of M1 and M2 macrophage polarization by *IL-6*, *IL-4*, *ARG-1*, *VEGF*, *CD163* and *IL-10*, (c) ICC results of M1/M2 polarization of control and GC/ZT-4 treated macrophages.

3.10. In vivo wound healing

Considering the positive *in vitro* results for GC/ZT-0 and GC/ZT-4 in skin cell proliferation, migration, and general cellular functions, we looked into this further in a male ICR rat model with a 1.2 cm subcutaneous skin wound (Fig. 12). According to the results, 94 % of the wound was effectively healed within 14 days of treatment (Fig. 12(a)). The wound healing area differed in the GC/ZT-0 and GC/ZT-4 compared to the control (Fig. 12(b)). On the 14th day, the epidermis in all groups was completely regenerated and began to form skin appendages, such as hair follicles (H) and blood vessels, in the dermis (E, D), especially in the two 3D-printed groups. The improved skin regeneration efficacy of GC/ZT-0 and GC/ZT-4 scaffolds is attributed to their better cellular activity, which facilitated skin cell proliferation and enhanced gene expression, as observed in *in vitro* results.

Histological analysis of the wound-tissue sections was performed after 14 days of scaffold implantation to observe epithelialization and new-tissue formation using H&E staining (Fig. 12(d)). The results indicate that the damaged epidermis was nearly healed in all the groups; however, a distinct epidermis layer of regular thickness was observed in the GC/ZT scaffold-treated groups. Additionally, the complete formation of the keratinized layer in the GC/ZT-4 implanted tissue suggests the completion of wound healing. H&E staining also revealed the construction of new tissue on the 14th day. A dense accumulation of fibroblasts increased the number of blood vessels in the dermis, and the skin structures were restored more rapidly in the GC/ZT-4 treated group than in the blank. The formation of hair follicles (H) in the deep epidermis (D) and superficial epidermis (E) was observed in the GC/ZT-4 treatment group. The higher regeneration ability of GC/ZT-4 scaffolds is attributed to their greater expression of different factors, including *Fibronectin* and *TGF-β1*. The upregulated gene expression of *Fibronectin* and *TGF-β1* is already shown in *in vitro* results. It is well known that *Fibronectin* plays an important role in tissue repair, adhesion, and migration of fibroblasts, endothelial cells, and immune cells such as neutrophils and monocytes (Grinnell, 1984; Wang et al., 2022). Similarly, *TGF-β1* is essential for granulation tissue formation, cell proliferation, differentiation, ECM production, modulation of immune response, and wound healing-promoting factor (Kiritsi & Nyström,

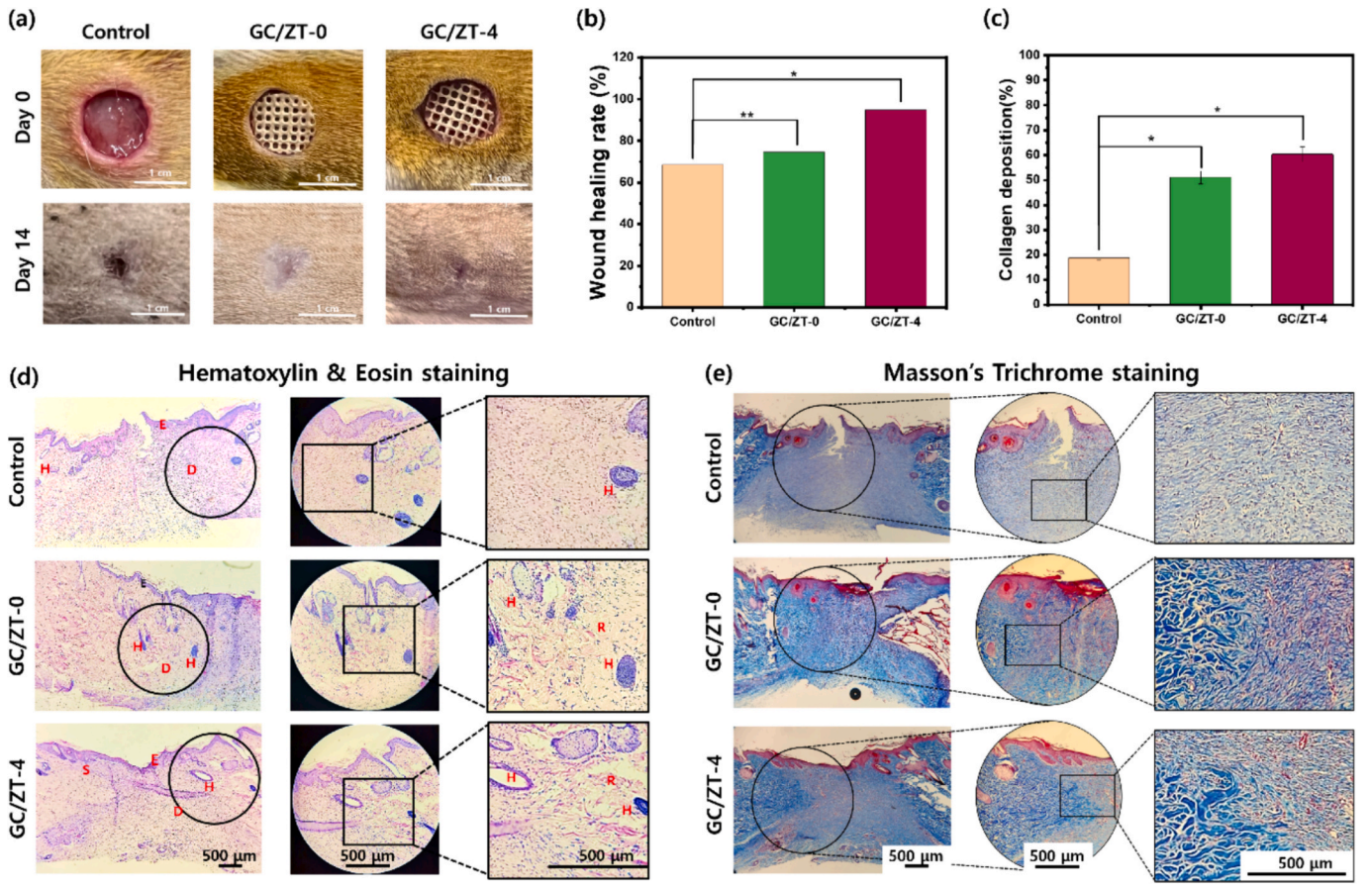

Fig. 12. (a) Digital photographs of wounds at day 0 and day 14 and (b) Their respective wound healing rate (c) *Collagen* deposition in percentage after day 14 (d) H&E staining results after 14 days of treatment, showing the presence of superficial epidermis (E), deep epidermis (D), hair follicle (H), sebaceous gland (S) and dermis inner reticular which comprises thick connective tissue; (e) MT staining results showing collagen deposition (blue stain) and presence of keratin (red stain) in control, GC/ZT-0 and GC/ZT-4 treatment groups.

2018; Pakyari et al., 2013; Ramirez et al., 2013). Hence, the upregulation of these genes could be the reason for effective wound healing in the *in vivo* investigation.

To further investigate the efficiency of the GC/ZT scaffolds in wound healing, *Collagen* deposition after 14 days of treatment was examined. The formation of *Collagen* at the wound site plays a vital role in remodeling damaged skin tissue, as assessed by Masson's trichrome staining (Zhang et al., 2021). *Collagen* is a key component in the extracellular matrix and plays a critical role in regulating the phases of wound healing (Sun, 2021). As shown in Fig. 12(d), *Collagen* deposition could not be seen in all groups. Less collagen deposition was found in the control group, while the GC/ZT-0 and GC/ZT-4 groups showed enhanced *Collagen* deposition with a better-organized fibrous structure. The image observation clearly shows in Fig. 12(e) that the *Collagen* densities in the GC/ZT-4 group were higher than those of the GC/ZT-0 group, and both treatment groups were higher than those of the control groups at the same time point (day 14). The quantitative graph is given in Fig. 12(c). These results confirmed that the maturation and remodeling stages were achieved. Table 1 shows various studies of chitosan-based hydrogels for antibacterial and biomedical applications.

4. Conclusion

Herein, we developed 3D printable multifunctional hydrogels using glycol-grafted chitosan, gelatin, and zinc-functionalized tannic acid for antibacterial effects and rapid wound healing. The glycol chitosan was synthesized with a one-step facile synthesis to overcome the limitations of mechanical strength and low solubility and enhance the bactericidal and anti-biofilm activity. The intermolecular bonds in hydrogel were strengthened by tannic acid to enhance the physiochemical properties, including viscoelasticity, adhesiveness, and recovery potential. GC/ZT-4 hydrogel showed outstanding adhesive strength (~210 kPa) and storage modulus. The hydrogels were easily printed and maintained their predesigned morphologies with glutaraldehyde crosslinking, demonstrating superior printability and stability. The hydrogels rapidly inhibited the growth of *B. subtilis* and *E. coli*, showing outstanding bactericidal effects and biofilm eradication. The hydrogels also exhibited excellent antioxidant properties, which can reduce oxidative stress in the infected areas. The hydrogels have no adverse effects on human dermal fibroblasts and promote the expression of wound healing genes, including (*Collagen*, *Fibronectin*, and *TGF-β1*) indicating their superior cytocompatibility and angiogenic potential, respectively. Rapid cell migration occurred with developed hydrogels, providing favorable conditions for enhanced cellular activity.

Furthermore, hydrogels favored M2 polarization of macrophage cells, which is essential for rapid wound healing. Faster wound healing was observed in subcutaneous rat wounds in hydrogel-treated groups compared to the control, and more significantly, ZnTA-added hydrogels (94 %), due to their improved cellular activity. Collectively, the current outstanding findings provide convincing results to show multifunctional GC/ZT hydrogel as a potential material for 3D printing, bacteria inhibition, biofilm eradication, M2 macrophage polarization, and skin tissue regeneration. These results also suggested that the developed hydrogels can be used as skin patches for bacteria-infected wounds for rapid healing. However, more studies on bacteria-infected wound healing must validate the findings and use the developed hydrogel platforms for

Table 1
Comparison of the present study with the previous studies related to chitosan-based hydrogels for antibacterial and biomedical applications.

Formulations	Major findings	Limitations	Applications	Reference
CMCA-DOHA-pDA@Raf hydrogel	Enhanced mechanical strength Rapid self-healing Antibacterial potential (*E. coli* 97.5 ± 4.1 %), and *S. aureus* (99.6 ± 3.1 %)	Poor adhesive strength (16 kPa)	Hemostasis and wound healing	(Wang, Gao, et al., 2024)
PCCS/Fe^{3+} hydrogel	Improved swelling efficiency Good adhesive strength (78 kPa) Antibacterial property *E. coli, and S. aureus* > 98 % Controlled release of Mg^{2+}	Low degradation rate	Hemostasis and wound healing	(Liu et al., 2023)
QCMOD-MINP hydrogel	Good Injectability Rapid self-healing Antibacterial potential (*E. coli*, and *S. aureus* >80 %)	Poor adhesive strength (8 kPa)	Bacteria-infected wound healing	(Liu, Zhao, et al., 2024)
LAMC-MoS_2@PDA hydrogel	Rapid cell migration and angiogenesis Superior photothermal property ROS scavenging activity Biocompatible	Moderate antibacterial potential without NIR (*E. coli*, and *S. aureus* ~ 30–40 %) Toxic byproducts generated due to MoS_2	Wound healing	(Wang, Liu, et al., 2024)
Alg/Chi – Neo hydrogel	High swelling efficiency Pharmacological stable >60 days Antibacterial potential (*S. aureus* > 95 %)	Cell viability decreased with time	Wound healing	(Silva et al., 2024)
CMCh(Fe^{3+} or Al^{3+}) hydrogel	Injectable and rapid self-healing Enhanced viscoelasticity Biocompatible Rapid angiogenesis	Poor adhesive strength (10.3 kPa)	Wound healing	(Cao et al., 2021)
CMCS/Fe^{3+}/CIP hydrogel	Good injectability and moldability Biocompatible Osteogenic potential Antibacterial property (*S. aureus* ~ 80 %)	Moderate bone regeneration efficiency (~54 % in 8 weeks)	Bone regeneration	(Zhou et al., 2024)
CPD hydrogel	Superior photothermal property Radical scavenging potential Biocompatible Rapid cell migration Antibacterial	Moderate viscoelasticity and mechanical strength	Bacteria infected wound healing	(Ouyang et al., 2024)
CMCs/Odex/CE hydrogel	Rapid gelation, and injectable Good photothermal activity Radical scavenging potential Biocompatible Antibacterial potential *(E. coli*, and *S. aureus* ~ 80.0 % without NIR)	Moderate adhesive strength (23.6 kPa)	Bacteria-infected wound healing	(Liu, Yu, et al., 2024)
GC/ZT 3D printable hydrogel	3D-printable Improved viscoelasticity and recovery strength Superior adhesive strength (210 kPa) Radical scavenging potential Biocompatible Rapid cell migration M2 macrophage polarization Rapid angiogenesis Antibacterial potential (*E. coli* > 93 %, and *B. subtilis* > 81 %)	–	Antibacterial, Antibiofilm, Wound healing	This study

CMCA – Arginine modified carboxymethyl chitosan; DOHA – dopamine modified oxidized hyaluronic acid; pDA – polydopamine; Raf – raffinose; PCCS – carboxylated PVA chitosan; QCM – methacrylic acid modified quaternerized chitosan with GTMAC powder; QCMOD-MINP – methacrylic acid modified quaternerized chitosan oxidized dextran,ar deti hu aaj MINP – MgO/Icariin; LAMC- lipoic acid on chitosan by amidation; MoS_2@PDA – Molybdenum disulfide modified polydopamine; Alg – alginate; Chi – chitosan; Neo – Neomycin; CMCh – carboxymethyl chitosan; CIP – ciprofloxacin; CPD – dopamine modified sodium alginate/carboxymethyl chitosan/polyvinylpyrrolidone; CE – cowberry extract; Odex – oxidized dextran.

practical applications.

Supplementary data to this article can be found online at https://doi.org/10.1016/j.carbpol.2024.122522.

CRediT authorship contribution statement

Tejal V. Patil: Writing – review & editing, Writing – original draft, Project administration, Methodology, Formal analysis, Data curation, Conceptualization. **Hexiu Jin:** Resources, Methodology, Formal analysis, Data curation. **Sayan Deb Dutta:** Writing – review & editing, Visualization, Validation, Supervision, Investigation. **Rumi Aacharya:** Visualization, Data curation. **Kehan Chen:** Visualization, Data curation. **Keya Ganguly:** Visualization. **Aayushi Randhawa:** Visualization. **Ki-Taek Lim:** Visualization, Validation, Supervision, Resources, Project administration, Funding acquisition.

Declaration of competing interest

The authors declare that no conflicts of financial interests or personal relationships have influenced the work reported in this paper.

Data availability

Data will be made available on request.

Acknowledgments

Funding: This study was supported by the 'Basic Science Research Program' through the 'National Research Foundation of Korea'funded by the 'Ministry of Education'(NRF-2018R1A16A1A03025582; NRF-2022R1I1A3063302). This work was supported by the Innovative Human Resource Development for Local Intellectualization program

through the Institute of Information & Communications Technology Planning & Evaluation (IITP) grant funded by the Korea government (MSIT) (IITP-2024-RS-2023-00260267).

References

Almoudi, M. M., Hussein, A. S., Abu Hassan, M. I., & Mohamad Zain, N. (2018). A systematic review on antibacterial activity of zinc against *Streptococcus mutans*. *The Saudi Dental Journal, 30*(4), 283–291.

Alsahag, M., Alisaac, A., Al-Hazmi, G. A. A., Pashameah, R. A., Attar, R. M. S., Saad, F. A., & El-Metwaly, N. M. (2023). Preparation of carboxymethyl cellulose/polyvinyl alcohol wound dressing composite immobilized with anthocyanin extract for colorimetric monitoring of wound healing and prevention of wound infection. *International Journal of Biological Macromolecules, 224*, 233–242.

Alvarez, K., & Nakajima, H. (2009 Jul 23). Metallic scaffolds for bone regeneration. *Materials (Basel), 2*(3), 790–832. https://doi.org/10.3390/ma2030790. eCollection 2009 Sep.

Andleeb, A., Mehmood, A., Tariq, M., Butt, H., Ahmed, R., Andleeb, A., … Riazuddin, S. (2022). Hydrogel patch with pretreated stem cells accelerates wound closure in diabetic rats. *Biomaterials Advances, 142*, Article 213150.

Arif, S., Attiogbe, E., & Moulin, V. J. (2021). Granulation tissue myofibroblasts during normal and pathological skin healing: The interaction between their secretome and the microenvironment. *Wound Repair and Regeneration, 29*(4), 563–572.

Bal-Ozturk, A., Cecen, B., Avci-Adali, M., Topkaya, S. N., Alarcin, E., Yasayan, G., … Hassan, S. (2021). Tissue adhesives: From research to clinical translation. *Nano Today, 36*.

Bigham, A., Rahimkhoei, V., Abasian, P., Delfi, M., Naderi, J., Ghomi, M., … Akbari, A. (2022). Advances in tannic acid-incorporated biomaterials: Infection treatment, regenerative medicine, cancer therapy, and biosensing. *Chemical Engineering Journal, 432*, Article 134146.

Bu, Y., & Pandit, A. (2022). Cohesion mechanisms for bioadhesives. *Bioactive Materials, 13*, 105–118.

Cao, H., Wang, J., Hao, Z., & Zhao, D. (2024). Gelatin-based biomaterials and gelatin as an additive for chronic wound repair. *Frontiers in Pharmacology, 15*.

Cao, J., Wu, P., Cheng, Q., He, C., Chen, Y., & Zhou, J. (2021). Ultrafast fabrication of self-healing and injectable Carboxymethyl chitosan hydrogel dressing for wound healing. *ACS Applied Materials & Interfaces, 13*(20), 24095–24105.

Chen, C., Yang, H., Yang, X., & Ma, Q. (2022). Tannic acid: A crosslinker leading to versatile functional polymeric networks: A review. *RSC Advances, 12*(13), 7689–7711.

Choi, G., & Cha, H. J. (2019). Recent advances in the development of nature-derived photocrosslinkable biomaterials for 3D printing in tissue engineering. *Biomaterials Research, 23*(1), 18.

Divyashri, G., Badhe, R. V., Sadanandan, B., Vijayalakshmi, V., Kumari, M., Ashrit, P., … Raghu, A. V. (2022). Applications of hydrogel-based delivery systems in wound care and treatment: An up-to-date review. *Polymers for Advanced Technologies, 33*(7), 2025–2043.

Dong, R., Li, Y., Chen, M., Xiao, P., Wu, Y., Zhou, K., … Tang, B. Z. (2022). In situ electrospinning of aggregation-induced emission nanofibrous dressing for wound healing. *Small Methods, 6*(5), Article 2101247.

Dutta, S. D., Patil, T. V., Ganguly, K., Randhawa, A., & Lim, K.-T. (2023). Unraveling the potential of 3D bioprinted immunomodulatory materials for regulating macrophage polarization: State-of-the-art in bone and associated tissue regeneration. *Bioactive Materials, 28*, 284–310.

Ehtesabi, H., & Massah, F. (2021). Improvement of hydrophilicity and cell attachment of polycaprolactone scaffolds using green synthesized carbon dots. *Materials Today Sustainability, 13*, Article 100075.

Farha, A. K., Yang, Q.-Q., Kim, G., Li, H.-B., Zhu, F., Liu, H.-Y., … Corke, H. (2020). Tannins as an alternative to antibiotics. *Food Bioscience, 38*, Article 100751.

Fernandes, L. L., Resende, C. X., Tavares, D. S., Soares, G. A., Castro, L. O., & Granjeiro, J. M. (2011). Cytocompatibility of chitosan and collagen-chitosan scaffolds for tissue engineering. *Polímeros, 21*, 1–6.

Fu, X., Yuan, S., Yang, F., Yu, H., Xie, Y., Guo, Y., & Yao, W. (2023). Characterization of the interaction between boscalid and tannic acid and its effect on the antioxidant properties of tannic acid. *Journal of Food Science, 88*(4), 1325–1335.

Grinnell, F. (1984). Fibronectin and wound healing. *Journal of Cellular Biochemistry, 26*(2), 107–116.

Han, H., Tang, L., Li, Y., Li, Y., Bi, M., Wang, J., … Mao, J. (2023). A multifunctional surgical suture with electroactivity assisted by oligochitosan/gelatin-tannic acid for promoting skin wound healing and controlling scar proliferation. *Carbohydrate Polymers, 320*, Article 121236.

He, X. Y., Sun, A., Li, T., Qian, Y. J., Qian, H., Ling, Y. F., … Qian, Z. (2020). Mussel-inspired antimicrobial gelatin/chitosan tissue adhesive rapidly activated in situ by H_2O_2/ascorbic acid for infected wound closure. *Carbohydrate Polymers, 247*, Article 116692.

Horn, M. M., Martins, V. C. A., & de Guzzi Plepis, A. M. (2009). Interaction of anionic collagen with chitosan: Effect on thermal and morphological characteristics. *Carbohydrate Polymers, 77*(2), 239–243.

Huang, Y., Chen, Y., Lu, Z., Yu, B., Zou, L., Song, X., … Ji, J. (2023). Facile synthesis of self-targeted Zn^{2+}-gallic acid nanoflowers for specific adhesion and elimination of gram-positive bacteria. *Small, 19*(43), Article 2302578.

Huang, Y., Lin, Q., Yu, Y., & Yu, W. (2020). Functionalization of wood fibers based on immobilization of tannic acid and in situ complexation of Fe (II) ions. *Applied Surface Science, 510*, Article 145436.

Jennifer Sallit, R. (2012). Rationale for zinc supplementation in older adults with wounds. *Annals of Long-Term Care, 20*(1).

Joorabloo, A., & Liu, T. (2022). Recent advances in nanomedicines for regulation of macrophages in wound healing. *Journal of Nanobiotechnology, 20*(1), 407.

Kang, J. I., & Park, K. M. (2021). Advances in gelatin-based hydrogels for wound management. *Journal of Materials Chemistry B, 9*(6), 1503–1520.

Kendall, R. T., & Feghali-Bostwick, C. A. (2014). Fibroblasts in fibrosis: Novel roles and mediators. *Frontiers in Pharmacology, 5*.

Kim, J., Lee, K., & Nam, Y. S. (2021). Metal-polyphenol complexes as versatile building blocks for functional biomaterials. *Biotechnology and Bioprocess Engineering, 26*(5), 689–707.

Kim, M., Njaramba, L. K., Yoon, Y., Jang, M., & Park, C. M. (2024). Thermally-activated gelatin-chitosan-MOF hybrid aerogels for efficient removal of ibuprofen and naproxen. *Carbohydrate Polymers, 324*, Article 121436.

Kiritsi, D., & Nyström, A. (2018). The role of TGFβ in wound healing pathologies. *Mechanisms of Ageing and Development, 172*, 51–58.

Lee, J. H. (2018). Injectable hydrogels delivering therapeutic agents for disease treatment and tissue engineering. *Biomaterials Research, 22*(1), 27.

Leite, L. S. F., Pham, C., Bilatto, S., Azeredo, H. M. C., Cranston, E. D., Moreira, F. K., … Bras, J. (2021). Effect of tannic acid and cellulose nanocrystals on antioxidant and antimicrobial properties of gelatin films. *ACS Sustainable Chemistry & Engineering, 9*(25), 8539–8549.

Leng, L., Xiong, Q., Yang, L., Li, H., Zhou, Y., Zhang, W., … Huang, H. (2021). An overview on engineering the surface area and porosity of biochar. *Science of the Total Environment, 763*, Article 144204.

Liu, C., Xu, Y., Lu, Y., Du, P., Li, X., Wang, C., … Lu, G. (2022). Mesenchymal stromal cells pretreated with proinflammatory cytokines enhance skin wound healing via IL-6-dependent M2 polarization. *Stem Cell Research & Therapy, 13*(1), Article 414.

Liu, K., Yu, Y., Zhao, H., Yang, M., Zhang, C., Guan, F., & Yao, M. (2024). Cowberry extract loaded chitosan hydrogel with photothermal and antioxidant properties promotes infected wound healing. *International Journal of Biological Macromolecules, 262*, Article 129988.

Liu, S., Li, D., Wang, Y., Zhou, G., Ge, K., & Jiang, L. (2023). Adhesive, antibacterial and double crosslinked carboxylated polyvinyl alcohol/chitosan hydrogel to enhance dynamic skin wound healing. *International Journal of Biological Macromolecules, 228*, 744–753.

Liu, W., Li, J., Cheng, M., Wang, Q., Yeung, K. W. K., Chu, P. K., & Zhang, X. (2018). Zinc-modified sulfonated Polyetheretherketone surface with immunomodulatory function for guiding cell fate and bone regeneration. *Advanced Science (Weinh), 5*(10), Article 1800749.

Liu, Y., Zhao, F., Song, T., Tang, M., Tian, L., He, T., … Zhang, X. (2024). Nanohybrid dual-network chitosan-based hydrogels: Synthesis, characterization, quicken infected wound healing by angiogenesis and immune-microenvironment regulation. *Carbohydrate Polymers, 325*, Article 121589.

Lobo, V., Patil, A., Phatak, A., & Chandra, N. (2010). Free radicals, antioxidants and functional foods: Impact on human health. *Pharmacognosy Reviews, 4*(8), 118–126.

Lou, W., Chen, Y., Ma, H., Liang, G., & Liu, B. (2018). Antioxidant and α-amylase inhibitory activities of tannic acid. *Journal of Food Science and Technology, 55*(9), 3640–3646.

Lu, J., Chen, Y., Ding, M., Fan, X., Hu, J., Chen, Y., … Liu, W. (2022). A 4arm-PEG macromolecule crosslinked chitosan hydrogels as antibacterial wound dressing. *Carbohydrate Polymers, 277*, Article 118871.

Mittal, M., Siddiqui, M. R., Tran, K., Reddy, S. P., & Malik, A. B. (2014). Reactive oxygen species in inflammation and tissue injury. *Antioxidants & Redox Signaling, 20*(7), 1126–1167.

Moeini, A., Pedram, P., Makvandi, P., Malinconico, M., & Gomez d'Ayala, G. (2020). Wound healing and antimicrobial effect of active secondary metabolites in chitosan-based wound dressings: A review. *Carbohydrate Polymers, 233*, Article 115839.

Mora, C., McKenzie, T., Gaw, I. M., Dean, J. M., von Hammerstein, H., Knudson, T. A., … Franklin, E. C. (2022). Over half of known human pathogenic diseases can be aggravated by climate change. *Nature Climate Change, 12*(9), 869–875.

Nagahama, H., Maeda, H., Kashiki, T., Jayakumar, R., Furuike, T., & Tamura, H. (2009). Preparation and characterization of novel chitosan/gelatin membranes using chitosan hydrogel. *Carbohydrate Polymers, 76*(2), 255–260.

Ning, L., Mehta, R., Cao, C., Theus, A., Tomov, M., Zhu, N., … Serpooshan, V. (2020). Embedded 3D bioprinting of gelatin methacryloyl-based constructs with highly tunable structural fidelity. *ACS Applied Materials & Interfaces, 12*(40), 44563–44577.

Osolnik, U., Vek, V., Korošec, R. C., Oven, P., & Poljanšek, I. (2024). Integration of wood-based components – Cellulose nanofibrils and tannic acid - into a poly(vinyl alcohol) matrix to improve functional properties. *International Journal of Biological Macromolecules, 256*, Article 128495.

Ouyang, Y., Su, X., Zheng, X., Zhang, L., Chen, Z., Yan, Q., … Wang, S. (2024). Mussel-inspired "all-in-one" sodium alginate/carboxymethyl chitosan hydrogel patch promotes healing of infected wound. *International Journal of Biological Macromolecules, 261*, Article 129828.

Pakyari, M., Farrokhi, A., Maharlooei, M. K., & Ghahary, A. (2013). Critical role of transforming growth factor Beta in different phases of wound healing. *Advances in Wound Care, 2*(5), 215–224.

Patel, D. K., Patil, T. V., Ganguly, K., Dutta, S. D., & Lim, K.-T. (2023). Nanocellulose-assisted 3D-printable, transparent, bio-adhesive, conductive, and biocompatible hydrogels as sensors and moist electric generators. *Carbohydrate Polymers, 315*, Article 120963.

Patil, T. V., Patel, D. K., Dutta, S. D., Ganguly, K., Randhawa, A., & Lim, K.-T. (2021). Carbon nanotubes-based hydrogels for bacterial eradiation and wound-healing applications. *Applied Sciences, 11*(20), Article 9550.

Pillai, M. M., Dandia, H., Checker, R., Rokade, S., Sharma, D., & Tayalia, P. (2022). Novel combination of bioactive agents in bilayered dermal patches provides superior wound healing. *Nanomedicine: Nanotechnology, Biology and Medicine, 40*, Article 102495.

Ramirez, H., Patel, S. B., & Pastar, I. (2013). The role of TGFβ signaling in wound epithelialization. *Advances in Wound Care, 3*(7), 482–491.

Rasheed, U., Ain, Q. U., Yaseen, M., Yao, X., & Liu, B. (2021). Synthesis and characterization of tannic acid pillared bentonite composite for the efficient adsorption of aflatoxins. *Colloids and Surfaces B: Biointerfaces, 202*, Article 111679.

ReAct. (2022). 7.7 million people die from bacterial infections every year. https://www.reactgroup.org/news-and-views/news-and-opinions/year-2022/7-7-million-people-die-from-bacterial-infections-every-year/#:~:text=7.7%20million%20deaths%20around%20the%20world%20were%20found%20linked%20to,leading%20cause%20of%20death%20globally. (Accessed 5 July 2023).

Rodrigues, C., de Mello, J. M. M., Dalcanton, F., Macuvele, D. L. P., Padoin, N., Fiori, M. A., … Riella, H. G. (2020). Mechanical, thermal and antimicrobial properties of chitosan-based-nanocomposite with potential applications for food packaging. *Journal of Polymers and the Environment, 28*(4), 1216–1236.

Sahli, C., Moya, S. E., Lomas, J. S., Gravier-Pelletier, C., Briandet, R., & Hémadi, M. (2022). Recent advances in nanotechnology for eradicating bacterial biofilm. *Theranostics, 12*(5), 2383–2405.

Sathishkumar, G., Gopinath, K., Zhang, K., Kang, E.-T., Xu, L., & Yu, Y. (2022). Recent progress in tannic acid-driven antibacterial/antifouling surface coating strategies. *Journal of Materials Chemistry B, 10*(14), 2296–2315.

Shankar, S., Jaiswal, L., Selvakannan, P. R., Ham, K. S., & Rhim, J. W. (2016). Gelatin-based dissolvable antibacterial films reinforced with metallic nanoparticles. *RSC Advances, 6*(71), 67340–67352.

Sharifi-Rad, M., Anil Kumar, N. V., Zucca, P., Varoni, E. M., Dini, L., Panzarini, E., … Sharifi-Rad, J. (2020). Lifestyle, oxidative stress, and antioxidants: Back and forth in the pathophysiology of chronic diseases. *Frontiers in Physiology, 11*.

Silva, L.d. S., Vila Nova, B. G., Sousa, C. E. M.d., Silva, R. G., Carvalho, L. R.d. S., Silva, I. S. S., … Nascimento da Silva, L. C. (2024). Fabrication and characterization of physically crosslinked alginate/chitosan-based hydrogel loaded with neomycin for the treatment of skin infections caused by *Staphylococcus aureus*. *International Journal of Biological Macromolecules, 271*, Article 132577.

Sun, B. (2021). The mechanics of fibrillar collagen extracellular matrix. *Cell Reports Physical Science, 2*(8), Article 100515.

Sutherland, T. E., Dyer, D. P., & Allen, J. E. (2023). The extracellular matrix and the immune system: A mutually dependent relationship. *Science, 379*(6633), Article eabp8964.

Tabriz, A. G., & Douroumis, D. (2022). Recent advances in 3D printing for wound healing: A systematic review. *Journal of Drug Delivery Science and Technology, 74*, Article 103564.

Tondera, C., Hauser, S., Krüger-Genge, A., Jung, F., Neffe, A. T., Lendlein, A., … Pietzsch, J. (2016). Gelatin-based hydrogel degradation and tissue interaction in vivo: Insights from multimodal preclinical imaging in immunocompetent nude mice. *Theranostics, 6*(12), 2114–2128.

Wang, X., Zhu, J., Liu, X., Zhang, H. J., & Zhu, X. (2020). Novel gelatin-based eco-friendly adhesive with a hyperbranched cross-linked structure. *Industrial & Engineering Chemistry Research, 59*(13), 5500–5511.

Wang, Y., Gao, H., Wang, X., Li, D., Zhang, W., Meng, X., … Meng, X. (2024). Dual cross-linked self-healing hydrogel enhanced by dopamine nanoparticles and raffinose for wound healing. *International Journal of Biological Macromolecules, 271*, Article 132615.

Wang, Y., Liu, K., Huang, K., Wei, W., Huang, Y., & Dai, H. (2024). Photothermal antibacterial MoS_2 composited chitosan hydrogel for infectious wound healing. *Biomaterials Advances, 156*, Article 213701.

Wang, Z., Qi, F., Luo, H., Xu, G., & Wang, D. (2022). Inflammatory microenvironment of skin wounds. *Frontiers in Immunology, 13*.

Xu, C., Zhang Molino, B., Wang, X., Cheng, F., Xu, W., Molino, P., … Wallace, G. (2018). 3D printing of nanocellulose hydrogel scaffolds with tunable mechanical strength towards wound healing application. *Journal of Materials Chemistry B, 6*(43), 7066–7075.

Yadav, M., Kaushik, B., Rao, G. K., Srivastava, C. M., & Vaya, D. (2023). Advances and challenges in the use of chitosan and its derivatives in biomedical fields: A review. *Carbohydrate Polymer Technologies and Applications, 5*, Article 100323.

Yang, N., Venezuela, J., Almathami, S., & Dargusch, M. (2022). Zinc-nutrient element based alloys for absorbable wound closure devices fabrication: Current status, challenges, and future prospects. *Biomaterials, 280*, Article 121301.

Yilmaz Atay, H. (2020 Mar 6). Antibacterial activity of chitosan-based systems. *Functional Chitosan*, 457–489. https://doi.org/10.1007/978-981-15-0263-7_15

Zaboon, M., Saleh, A., & Al-Lami, H. (2019). Comparative cytotoxicity and genotoxicity assessments of chitosan amino acid derivative nanoparticles toward human breast cancer cell lines. *Egyptian Journal of Chemistry, 62*(11), 2061–2075.

Zhang, J.-N., Zhu, H., Liu, T., Chen, Y., Jiao, C., He, C., & Wang, H. (2020). Strong adhesion of hydrogels by polyelectrolyte adhesives. *Polymer, 206*, Article 122845.

Zhang, M., Li, X. H., Gong, Y. D., Zhao, N. M., & Zhang, X. F. (2002). Properties and biocompatibility of chitosan films modified by blending with PEG. *Biomaterials, 23*(13), 2641–2648.

Zhang, Z., Li, W., Liu, Y., Yang, Z., Ma, L., Zhuang, H., … Chang, J. (2021). Design of a biofluid-absorbing bioactive sandwich-structured Zn-Si bioceramic composite wound dressing for hair follicle regeneration and skin burn wound healing. *Bioactive Materials, 6*(7), 1910–1920.

Zhang, Z., Zhang, Q., Gao, S., Xu, H., Guo, J., & Yan, F. (2023). Antibacterial, anti-inflammatory and wet-adhesive poly(ionic liquid)-based oral patch for the treatment of oral ulcers with bacterial infection. *Acta Biomaterialia, 166*, 254–265.

Zhou, T., Zhou, H., Wang, F., Zhang, P., Shang, J., & Shi, L. (2024). An injectable carboxymethyl chitosan hydrogel scaffold formed via coordination bond for antibacterial and osteogenesis in osteomyelitis. *Carbohydrate Polymers, 324*, Article 121466.